AGU100 ADVANCING EARTH AND SPACE SCIENCE

Global Biogeochemical Cycles

RESEARCH ARTICLE

10.1029/2018GB005985

Key Points:

- The ^{238}U-^{234}Th method is used for the first time at the basin scale to estimate surface ocean export and residence times of trace metals
- Particulate flux patterns reflect nutrient-like (cadmium), nutrient-scavenging (cobalt), and scavenging-redox (manganese) trace metal types
- Residence times, with respect to the sinking flux at 100 m, were on the order of months to years for these trace metals and phosphorus

Supporting Information:

- Supporting Information S1

Correspondence to:
E. E. Black,
eblack@dal.ca

Citation:
Black, E. E., Lam, P. J., Lee, J.-M., & Buesseler, K. O. (2019). Insights from the ^{238}U-^{234}Th method into the coupling of biological export and the cycling of cadmium, cobalt, and manganese in the Southeast Pacific Ocean. *Global Biogeochemical Cycles*, *33*, 15–36. https://doi.org/10.1029/2018GB005985

Received 23 MAY 2018
Accepted 6 DEC 2018
Accepted article online 10 DEC 2018
Published online 8 JAN 2019

Insights From the ^{238}U-^{234}Th Method Into the Coupling of Biological Export and the Cycling of Cadmium, Cobalt, and Manganese in the Southeast Pacific Ocean

E. E. Black[1,2], P. J. Lam[3], J.-M. Lee[3], and K. O. Buesseler[2]

[1]Ocean Frontier Institute, Dalhousie University, Halifax, Nova Scotia, Canada, [2]Department of Marine Chemistry and Geochemistry, Woods Hole Oceanographic Institution, Woods Hole, MA, USA, [3]Ocean Sciences Department, Institute of Marine Sciences, University of California, Santa Cruz, CA, USA

Abstract Better constraints on the magnitude of particulate export and the residence times of trace elements are required to understand marine food web dynamics, track the transport of anthropogenic trace metals in the ocean, and improve global climate models. While prior studies have been successful in constructing basin-scale budgets of elements like carbon in the upper ocean, the cycling of particulate trace metals is poorly understood. The ^{238}U-^{234}Th method is used here with data from the GP-16 GEOTRACES transect to investigate the upper ocean processes controlling the particulate export of cadmium, cobalt, and manganese in the southeastern Pacific. Patterns in the flux data indicated that particulate cadmium and cobalt behave similarly to particulate phosphorus and organic carbon, with the highest export in the productive coastal region and decreasing flux with depth due to remineralization. The export of manganese was influenced by redox conditions at the low oxygen coastal stations and by precipitation and/or scavenging elsewhere. Residence times with respect to export (total inventory divided by particulate flux) for phosphorus, cadmium, cobalt, and manganese in the upper 100 and 200 m were determined to be on the order of months to years. These GEOTRACES-based synthesis efforts, combining a host of concentration and tracer data with unprecedented resolution, will help to close the oceanic budgets of trace metals.

Plain Language Summary Despite trace metals being present at low concentrations in the ocean, they can be essential to many cellular functions for marine organisms. The abundance of these metals can impact marine food webs and, therefore, how we construct global models for simulating past, current, and future ocean conditions. To improve our understanding of the interactions between ocean biology and metals, we need a better understanding of the comparative sources of these metals, such as dust and rivers, and the interior biological, oxidation-reduction, and scavenging sinks. In particular, we need to know how much of a given metal is being transported out of the upper ocean via sinking particles. Once a particle reaches a depth of a few hundred meters, the attached metals will remain in the deep ocean for hundreds of years to millennia, where they will be unavailable for use by surface organisms. In this study we focus on measuring the quantity of particle-associated cadmium, cobalt, and manganese leaving the surface ocean daily in the southeastern tropical Pacific. We also include a comparison with patterns observed in organic carbon and phosphorus, which are more traditionally studied biological components that are present in much higher concentrations in the marine environment.

1. Introduction

1.1. Constraining the Particulate Export of Trace Metals

The cycling of trace metals (TM) in the marine environment has long been an important area of study because TM are essential to marine ecosystems, impact the exchange of nutrients to deeper waters and can affect global trends in ocean productivity and climate change (Martínez-García et al., 2014; Morel et al., 2004; Morel & Price, 2003; Sunda & Huntsman, 1997; Watson et al., 2000). Cobalt (Co) has been shown to be colimiting to phytoplankton growth (Saito & Goepfert, 2008) and manganese (Mn) is utilized in enzymes and as an electron acceptor or donor for marine bacteria (Moffett & Ho, 1996; Morel & Price, 2003; Tebo et al., 1984). It is also vital to understand the mechanisms for the delivery of nutrient proxies to the deep ocean,

such as Cd, whose distribution in the marine environment is well correlated with phosphorus (Boyle, 1988; Elderfield & Rickaby, 2000; Horner et al., 2013). In addition, the geochemical fates of anthropogenic contaminants, such as mercury or cesium, influence the health of ocean ecosystems and our decision making on the safe utilization of ocean resources (Buesseler et al., 2012; Lamborg et al., 2014).

Better estimates of TM fluxes are needed to advance ocean biogeochemical general circulation models (OBGCMs) and our overall understanding of TM cycling. A recent comparison of 13 Fe-incorporating OBGCMs found that "all models struggle to reproduce many aspects of the observed spatial patterns" (Tagliabue et al., 2016) and the first OBGCM for Mn cannot recreate observed distributions in the Pacific oxygen minimum zone or OMZ (van Hulten et al., 2017). One of the most important fluxes to constrain is particulate export out of the surface ocean, a major process in the internal cycling of TM and the first step to transporting TM to the deep ocean and sediments, which can act as a long-term sink. TM can move from the surface to the deep ocean via large-scale water mass mixing (centennial to millennial time scales) or by association with sinking particles (days to months). Because particle cycling impacts TM distributions within the ocean over relatively short time scales, particulate flux estimates are essential to interpreting observed patterns.

One of the primary methods to directly determine particulate export has been the utilization of sediment traps (e.g., Benitez-Nelson et al., 2007), although only a few shallow trap (less than 500-m depth) measurements of TM fluxes, such as Al, Fe, and Pb, had been made prior to the mid-2000s (Weinstein & Moran, 2005). These trap studies were also limited to distinct biogeochemical regions, such as the Mediterranean Sea (Migon et al., 2002; Quetel et al., 1993), the Ross Sea (Collier et al., 2000), the Northeastern Pacific (Landing & Bruland, 1987), and the Greenland Sea (Schüßler et al., 1997). The number of TM export estimates has increased in recent years (e.g., Bowie et al., 2009; Pohl et al., 2004; Stanley et al., 2004) although often for a select group of metals, such as barium (Dehairs et al., 2000; Dymond & Collier, 1996; Jeandel et al., 2000; McManus et al., 2002) and with relatively large uncertainties (Lamborg et al., 2008; Noble et al., 2012).

The other established technique for measuring particulate export is the ^{234}Th-^{238}U disequilibrium method (e.g., Benitez-Nelson et al., 2001; Buesseler et al., 1992). ^{234}Th, with a half-life of 24.1 days, is highly particle reactive and its disequilibrium with ^{238}U reflects processes acting on time scales of days to weeks. ^{238}U (t½ = 4.47 billion years) behaves conservatively with respect to salinity in the ocean (Not et al., 2012; Owens et al., 2011). Although ^{234}Th is found to be at equilibrium with ^{238}U throughout much of the water column, rapidly sinking particles in the surface ocean create a quantifiable deficit in ^{234}Th when they carry attached ^{234}Th to depth more quickly than ^{234}Th is created by ^{238}U decay. A deficit or excess of ^{234}Th relative to its parent is used with the ratio of an element or component to ^{234}Th on sinking particles at a given depth to determine a flux of that element (Buesseler et al., 1992, 2006). While only a few studies to date have applied the ^{234}Th method to estimate particulate TM fluxes, these efforts have provided some of the first constraints on Fe and Pb cycling near the North American coastline (Smith et al., 2014; Weinstein & Moran, 2005) and on Fe budgets in island-influenced regions of the Southern Ocean (Lemaitre et al., 2016; Planquette et al., 2011).

1.2. TM and Constituents of Interest

^{234}Th-based particulate fluxes and upper ocean residence times have been evaluated for three biologically relevant TM: Cd, Co, and Mn. These TM are diverse in the extent to which their oceanic distributions are impacted by dust sources, lateral inputs, surface production, remineralization, scavenging, and redox processes. This study provides a unique opportunity to broaden our knowledge of the factors impacting TM cycling and examine the application of the ^{234}Th-^{238}U method to TM for which little or no ^{234}Th-based particulate export estimates exist (Figure S1 in the supporting information). Export estimates for phosphorus (P) and carbon (C), specifically particulate organic carbon (POC), have been included to provide nutrient-like end-members for comparison.

The oceanic distributions of C and P reflect significant involvement in the internal cycling of biological particulate matter. P has low dissolved concentrations (P_{Diss}) in the surface, due to uptake, and increasing concentrations with depth as remineralization returns the nutrient to the dissolved phase (Bruland & Lohan, 2003). Both POC and particulate P are greatest in surface waters, where productivity is high, and decrease in concentration with depth. Cd has an oceanic distribution and residence time (full ocean inventory/all ocean inputs ~50 kyr) that most closely matches those of macronutrients like P (~53 kyr; Moore et al., 2013). While lateral

inputs from productive coastal waters and upwelling can supply Cd to the global ocean's gyres, dust is not thought to be a substantial source of Cd to the surface ocean (Bruland et al., 1994).

In contrast, the full ocean residence time of Mn is estimated to be only 60 years (Moore et al., 2013) and Mn_{Diss} generally decreases with depth, creating scavenged-type profiles. These characteristics reflect strong particle interactions, such as the sorption of Mn(II) onto sinking particles or the oxidation of Mn(II) and subsequent precipitation to form Mn oxides, that produce distinctly nonnutrient distributions. In OMZs, however, the formation of insoluble Mn oxides in the water column can be slower, resulting in a broad, dissolved subsurface maximum in the upper 2,000 m. Furthermore, in the suboxic cores of these OMZs, Mn oxides on settling particles are reductively dissolved (Ohnemus et al., 2016). Mn in the surface ocean is sourced from sediments, dust, and rivers; however, dust inputs are estimated to be much lower in the Pacific than the Atlantic (Jickells et al., 2005).

Co, with its centennial time scale ocean residence time (Moore et al., 2013), has a "hybrid" Co_{Diss} distribution that reflects both nutrient-like and scavenged properties. Co_{Diss} is generally low in the surface ocean due to uptake, but Pacific Co concentrations generally decrease with depth over the full water column and are lower than in the Atlantic. Mn-oxidizing bacteria are thought to facilitate the removal of Mn_{Diss} and Co_{Diss} from the water column via the biotic oxidation or coprecipitation of these two metals (Moffett & Ho, 1996; Tebo et al., 1984), producing scavenged-type distributions in the midwater column. Unlike Mn_{Diss}, Co_{Diss} profiles do not generally reflect atmospheric inputs, except in the high dust flux regions of the Atlantic (Dulaquais et al., 2014).

2. Materials and Methods

2.1. Sample Collection and Analysis

Between 29 October and 18 December 2013 on the GEOTRACES GP-16 cruise ("the transect"; 10–16°S and 77–152°W), samples for dissolved parameters ($_{Diss}$), total ^{234}Th, and high-volume particulate samples were collected from the upper 400 m at 21 stations (Figure 1). Detailed methods for the measurement and analyses of ^{234}Th (Black et al., 2018), size-fractionated particulate TM (see supporting information Text S1 and Lee et al., 2018), particle composition (Lam et al., 2018), and salinity (Moffett et al., 2014) have been published previously and all data are available through BCO-DMO (see Website and Database References; Buesseler et al., 2016, 2017; Lam, 2017). In summary, total ^{234}Th was sampled using a standard rosette. McLane in situ pumps were used to collect ^{234}Th, POC, P, and TM particulates (Bishop et al., 2012; Lam et al., 2018). Each pump system contained two filter heads. One head contained a polyester prefilter (>51 μm) and a pair of QMA filters (>1 μm) and the other a prefilter and a pair of 0.8-μm Supor filters (Lee et al., 2018). Small particle (SP) ^{234}Th and POC (1–51 μm) were measured on a 25-mm punch of the QMA. Material from the Supor-side prefilter was used to quantify large particle (LP; >51 μm) ^{234}Th and POC. Wedges of the Supor and QMA-side prefilter were used for TM_{SP} and TM_{LP} measurements, respectively.

2.2. Biogeochemical Regions

Results of this study are discussed relative to three zones (Figure 1): the Shelf (77–80°W), the Offshore (80–100°W), and the Gyre (100–152°W). The Shelf is an upwelling-influenced, highly productive coastal zone, while the Gyre is an open ocean, low-nutrient, subtropical gyre. The local gyre has an OMZ where dissolved oxygen drops to detectable minima (4% to 29% oxygen saturation) due to weak ventilation and the respiration of sinking organic matter (Karstensen et al., 2008). The average depth of these minima was 340 m, which was well below the average depth of the base of the euphotic zone (E_z; determined from fluorescence by Ohnemus et al., 2016) of 170 m. The Shelf and Offshore, on the other hand, had oxygen-deficient waters (ODZ) starting at an average depth of 50 and 150 m, respectively, where the average E_z depths were 40 and 120 m, respectively. Here the concentration of oxygen dropped below detection using traditional methods ($O_2 < 1$ μM) and the upper boundary of the ODZ (uODZ; Black et al., 2018) indicates the approximate depth of change to oxygen-deficient redox conditions in the water column. The ODZ waters thinned from ~700 m below the uODZ in the Shelf to ~150 m in the Offshore.

2.3. ^{234}Th-^{238}U Method for TM Flux Determination

The particulate flux of ^{234}Th in disintegrations per minute (dpm) per liter per day can be calculated at depth z with the following relationship:

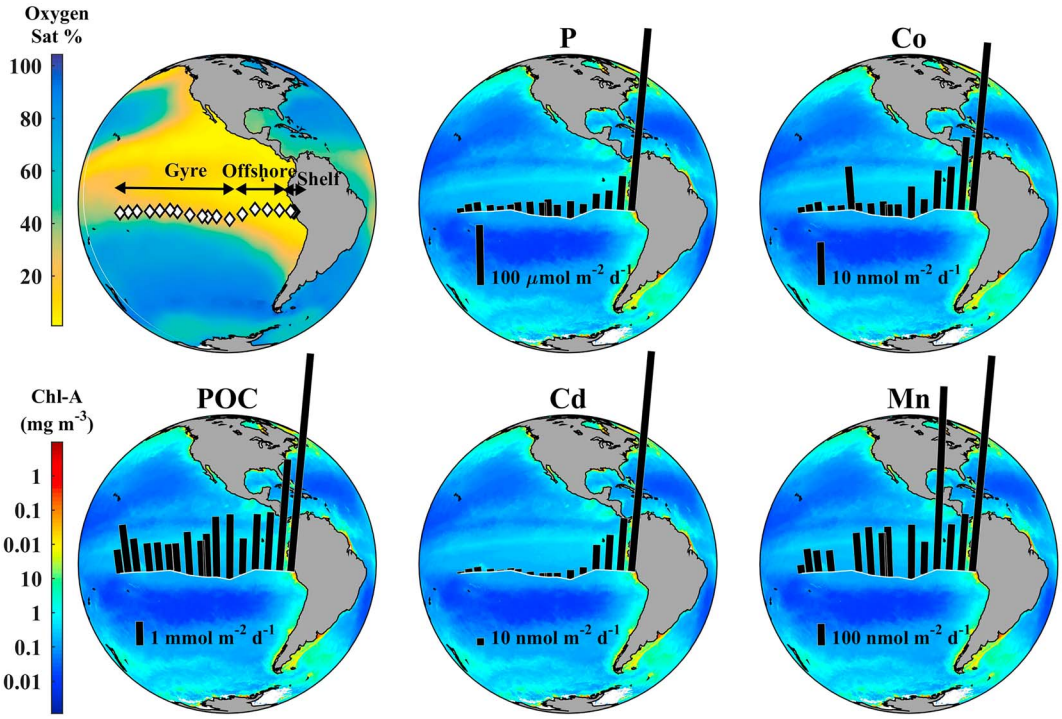

Figure 1. Zonal boundaries and particulate trace metal fluxes at 100 m. The three zones are shown in the first map overlying oxygen saturation percent at 400 m (NOAA World Ocean Atlas, 2009). In the remaining maps, the annual chlorophyll *a* concentration (colors; NASA, 2018) for 2015 is shown with particulate export at 100 m (bars). For the Shelf region (stations 1 to 5), the mean flux is shown with a single bar. POC = particulate organic carbon.

$$P_{\mathrm{Th}@z} = \int_0^z \left(\lambda_{\mathrm{Th}} \left({}^{238}\mathrm{U} - {}^{234}\mathrm{Th} \right) + w\frac{\partial {}^{234}\mathrm{Th}}{\partial z} - u\frac{\partial {}^{234}\mathrm{Th}}{\partial x} - v\frac{\partial {}^{234}\mathrm{Th}}{\partial y} \right) \mathrm{d}z \quad (1)$$

where ^{234}Th is the total ^{234}Th activity (dpm/L), ^{238}U is the salinity-derived ^{238}U activity, λ_{Th} is the decay constant (0.0288 day^{-1}), w is the upwelling velocity, u is the zonal velocity, v is the meridional velocity, and the gradients (∂^{234}Th terms) are vertical, west to east, and south to north, respectively. If the upwelling, zonal, and meridional terms are determined to be negligible and the system is assumed to be in steady state, the flux can be calculated using a simplified equation:

$$P_{\mathrm{Th}@z} = \int_0^z \lambda_{\mathrm{Th}} \left({}^{238}\mathrm{U} - {}^{234}\mathrm{Th} \right) \mathrm{d}z \quad (2)$$

For most stations, the particulate flux of ^{234}Th was found using equation (2). However, the locations between 77 and 84°W were determined to be impacted by upwelling (Kadko, 2017) and all ^{234}Th fluxes used here for this region have been corrected for these effects (Black et al., 2018). The high-resolution measurements here allow for the calculation of ^{234}Th flux at any depth by linear extrapolation between sampled depths.

Although the ^{234}Th method has infrequently been used to calculate fluxes for particulate components other than carbon or macronutrients (e.g., nitrogen and biogenic silica), the technique can be applied to determine the flux of any particulate component at depth z with the following equation:

$$P_{\mathrm{Comp}@z} = [\mathrm{Component}]^{234}\mathrm{Th} P_{\mathrm{Th}@z} \quad (3)$$

where the ratio of the component concentration to the ^{234}Th activity on large, "sinking" particles is multiplied by the particulate flux of ^{234}Th at depth z (see Text S2 for additional information on particle ratio calculations and uncertainties). We use "export" interchangeably with "particulate flux," and since ^{234}Th is the only isotope of thorium used in this study, ratios will be abbreviated as Comp:Th (e.g., cobalt:^{234}Th as Co:Th). It is assumed that the $\mathrm{Comp_{LP}}$:$\mathrm{Th_{LP}}$ (>51 μm) measured at z is representative of the ratio of sinking particles (Buesseler

et al., 2006). Particulate fluxes have been calculated at 100 m, 200 m, the uODZ, and at 100 m below the uODZ. The 100-m flux is of particular importance because this region of the Pacific is strongly stratified (strong halocline) and winter mixed layers do not generally reach deeper than 100 m (Fiedler & Talley, 2006). Therefore, any flux passing through 100-m depth is likely sequestered on greater than annual time scales.

The fraction of the TM concentration that was attributable to a lithogenic origin or to a combination of biological processes and authigenic precipitation ("bio-authigenic") was also determined. Average upper continental crust ratios were multiplied by the particle concentration of Al in a given sample to calculate the lithogenic fraction and the remainder was attributed to bio-authigenic processes. The mol:mol ratios used included Cd:Al = 2.93×10^{-7}, Co:Al 5.7×10^{-5}, P:Al 7.58×10^{-3}, and Mn:Al 3.67×10^{-3} (Taylor & McLennan, 1995). It should be noted that there can be regional deviations from the average crustal ratios and these differences have not been assessed here. The derived percentage of the total flux that was attributed to a lithogenic origin was reported (Table 1).

2.4. Calculation of Residence Times With Respect to Particle Export

The removal time scale or residence time τ of a particulate component with respect to export can be determined by

$$\tau_{\mathrm{Comp}} = \frac{I_{\mathrm{Comp}}}{P_{\mathrm{Comp}@z}} \tag{4}$$

where I is the water column inventory (moles/m^2) for a given depth region. The I used here are total water column inventories (I_{Tot}; sum of dissolved and particulate phases) and large particle inventories (I_{LP}). The application of specific values for I in equation (4) yields removal time scales relative to the total (τ_{Tot}) and large particle (τ_{LP}) pools of a given component. Dissolved concentrations utilized here were obtained from BCO-DMO (Hawco et al., 2016; John, 2015; John et al., 2018; Resing et al., 2015; Resing & Sedwick, 2016; Saito, 2016). Since sampling equipment was not deployed shallower than ~20 m, the inventory for the surface layer is assumed to be the same as the topmost sample and was integrated as such.

3. Results

3.1. Large Particle Concentrations

The large particle concentration data for all constituents have been reported and discussed previously (Lam et al., 2018; Lee et al., 2018). In this section, we briefly describe the patterns observed in the large particle concentration data, focusing on the upper 400 m. For reference, these data are rereported and grouped by zone in Figure S2.

POC_{LP} and P_{LP} decreased nonlinearly with depth from the base of the mixed layer (MLD) to 400 m. Production of POC and particulate P by phytoplankton in the surface and remineralization of sinking particles at depth translated to increasing dissolved and decreasing particulate concentrations with depth. POC_{LP} and P_{LP} just below the MLD decreased by an order of magnitude from the Shelf to the Gyre, although POC_{LP} in all three zones converged below 200 m (0.01–0.1 μM).

Cd_{LP} and Co_{LP} also varied by an order of magnitude just below the MLD from the Shelf to the Gyre. As expected from the tight coupling of global Cd_{Diss} and P_{Diss} concentrations (de Baar et al., 1994), Cd_{LP} profiles closely paralleled those of P_{LP}. Compared to POC_{LP}, P_{LP}, and Cd_{LP} profiles, Co_{LP} showed a more gradual decrease with depth in the Shelf and Offshore. In the Gyre, Co_{LP} below the MLD decreased until around 200 m, where concentrations began to increase with depth. A secondary maximum in the total particulate Co concentrations was noted by Lee et al. (2018) at stations west of 100°W and at depths ranging from 250 to 500 m.

Mn_{LP} profiles deviated the most from those of the other components. The effects of the dissolution of Mn oxides by photo-produced H_2O_2 (insoluble Mn reduced to dissolvable forms of Mn) was visible in the low concentrations of Mn_{LP} in the surface (Lee et al., 2018). Below the MLD, particulate Mn increased in the shelf and offshore until the uODZ was reached. This increase has been attributed to the precipitation of Mn oxyhydroxides by Mn-oxidizing bacteria (Cowen & Bruland, 1985; Lee et al., 2018; Ohnemus et al., 2016).

Table 1
^{234}Th-Derived Particulate Fluxes and Residence Time Estimates

		Shelf		Offshore		Gyre	
		n	Mean ± SEM (SD)	*n*	Mean ± SEM (SD)	*n*	Mean ± SEM (SD)
Particulate flux at 100 m	POC (mmol·m^{-2}·day^{-1})	5	9 ± 1 (3)	4	3 ± 1 (1)	12	1.6 ± 0.3 (1)
	P (μmol·m^{-2}·day^{-1})	5	300 ± 100 (342)	4	30 ± 10 (17)	12	17 ± 2 (8)
	Cd (nmol·m^{-2}·day^{-1})	5	300 ± 200 (400)	4	40 ± 20 (25)	12	5.4 ± 0.9 (3)
	Co (nmol·m^{-2}·day^{-1})	5	40 ± 9 (21)	4	10.0 ± 3 (6)	12	3.3 ± 0.9 (3)
	Mn (nmol·m^{-2}·day^{-1})	5	1000 ± 400 (1203)	4	400 ± 200 (315)	9	160 ± 20 (73)
Particulate flux at 200 m	POC (mmol·m^{-2}·day^{-1})	3	8 ± 0.6 (1)	4	1.5 ± 0.5 (1)	11	1.0 ± 0.1 (0.3)
	P (μmol·m^{-2}·day^{-1})	3	110 ± 50 (83)	4	14 ± 5 (14)	12	11 ± 3 (9)
	Cd (nmol·m^{-2}·day^{-1})	3	80 ± 40 (69)	4	20 ± 10 (22)	12	3.5 ± 0.6 (2)
	Co (nmol·m^{-2}·day^{-1})	3	30 ± 10 (23)	4	4 ± 2 (3)	12	3.3 ± 0.6 (2)
	Mn (nmol·m^{-2}·day^{-1})	3	400 ± 200 (335)	3	100 ± 50 (90)	12	700 ± 100 (391)
Particulate flux ratio $\left(\frac{\text{Flux at 200 m}}{\text{Flux at 100 m}}\right)$	POC	3	1.1 ± 0.2 (0.4)	4	0.5 ± 0.2 (0.3)	11	0.7 ± 0.1 (0.2)
	P	3	0.5 ± 0.3 (0.5)	4	0.5 ± 0.3 (0.5)	12	0.6 ± 0.1 (0.3)
	Cd	3	0.5 ± 0.3 (0.5)	4	0.6 ± 0.4 (0.7)	12	0.7 ± 0.1 (0.3)
	Co	3	1.0 ± 0.1 (0.1)	4	0.5 ± 0.2 (0.3)	12	1.3 ± 0.2 (0.6)
	Mn	3	0.6 ± 0.2 (0.4)	3	0.3 ± 0.2 (0.3)	12	4.9 ± 0.4 (1.5)
Lithogenic percent of flux at 100 m	P	5	0 ± 0% (0%)	4	0 ± 0% (0%)	9	0 ± 0% (0%)
	Cd	5	0 ± 0% (0%)	4	0 ± 0% (0%)	9	0 ± 0% (0%)
	Co	5	9 ± 4% (8%)	3	1.5 ± 0.6% (1%)	9	0.8 ± 0.3% (1%)
	Mn	5	50 ± 20% (45%)	3	4 ± 2% (4%)	10	2 ± 2% (5%)
τ_{LP} = I_{LP}/flux at 100 m (days)	POC	5	4.9 ± 0.9 (2)	4	15 ± 4 (7)	12	9 ± 1 (4)
	P	5	7 ± 4 (8)	4	16 ± 3 (5)	12	12 ± 2 (6)
	Cd	5	10 ± 4 (10)	4	16 ± 2 (3)	11	10 ± 1 (4)
	Co	5	5 ± 1 (3)	4	13 ± 2 (4)	12	9 ± 1 (5)
	Mn	5	6 ± 2 (4)	4	6 ± 1 (2)	9	4 ± 1 (3)
τ_{Tot} = I_{Tot}/flux at 100 m (years)	P	5	4 ± 2 (4)	4	9 ± 1 (2)	12	7 ± 0.9 (3)
	Cd	4	2 ± 1 (2)	4	1.0 ± 0.3 (0.6)	10	0.6 ± 0.2 (0.6)
	Co	5	1.3 ± 0.3 (0.7)	4	2.4 ± 0.5 (0.9)	12	1.7 ± 0.3 (1)
	Mn	5	1.5 ± 0.4 (1)	4	3 ± 1 (2)	8	1.9 ± 0.3 (0.9)

Note. Mean values for each zone are reported with standard deviations (SD), number of stations used in the calculations (*n*), and the standard errors of the mean (SEM = SD/$\sqrt{n}$). SD are original and have not been rounded for significant figures. Residence times are calculated using 0- to 100-m inventories (I_{LP} or I_{tot}) and are determined with respect to particulate export (see section 2.4). POC = particulate organic carbon.

Low particulate Mn concentrations within the ODZ indicated that the particulate Mn (Mn oxyhydroxides) was reduced below the uODZ, which is consistent with the observation of other reduced species, such as nitrite, Fe(II), and iodide (Cutter et al., 2018). In the Gyre, Mn_{LP} started low at the MLD and increased with depth until 300 m, except at 3 of the 12 stations (125°W, 128°W, and 137°W). At these locations, a larger, shallower maximum was observed just above the E_z.

3.2. Component to ^{234}Th Ratios

POC_{LP}:Th_{LP} decreased with depth in the upper 400 m (Table 2) and peaks in POC_{LP} and $^{234}Th_{LP}$ often coincided (see Figure S3 for a visual representation of MLD to 400-m Comp:Th for all components). The average POC_{LP}:Th_{LP} in the upper 100 m of each zone ranged from 2 μmol/dpm (Offshore and Gyre) to 5 μmol/dpm (Shelf). At depths below 100 to 400 m, zonal means ranged from 0.7 to 1.3 μmol/dpm. The transect range in POC_{LP}:Th_{LP} for the upper 400 m was 0.1–19 μmol/dpm. In the Shelf, in particular, the 19-fold difference between the lowest and highest value observed in the upper 100 m was much smaller than the 70- to 120-fold differences seen for other components.

P_{LP}:Th_{LP} profiles also decreased with depth (Table 2), although the few nonsurface P_{LP} peaks that were observed resulted in pronounced maxima in P_{LP}:Th_{LP} at five locations in the Offshore and Gyre. The means for the upper 100 m ranged from 19 nmol/dpm in the Gyre to 140 nmol/dpm in the Shelf and the transect range was 0.3–600 nmol/dpm. The gradient in the upper 100 m from the Shelf to the Offshore was greater for P_{LP}:Th_{LP} than all other components and was reflected in the 75% decrease between the means.

Table 2
Large Particle Component to ^{234}Th Ratio Statistics

	Shelf			Offshore			Gyre		
	Mean (SD)	*n*	Range	Mean (SD)	*n*	Range	Mean (SD)	*n*	Range
POC:Th (μmol:dpm), 0–100 m	5 (5)	15	1–19	2 (1)	9	1–3	2 (1)	30	0.1–3
POC:Th (μmol:dpm), 100–400 m	1.3 (0.3)	11	1–2	1.0 (0.2)	16	0.7–2	0.7 (0.2)	35	0.3–2
P:Th (nmol:dpm), 0–100 m	140 (150)	16	5–600	35 (20)	9	11–72	19 (9)	30	0.3–35
P:Th (nmol:dpm), 100–400 m	23 (16)	11	8–54	8 (6)	16	3–27	6 (5)	36	2–28
Cd:Th (pmol:dpm), 0–100 m	140 (150)	16	6–560	44 (32)	8	5–93	7 (9)	28	2–49
Cd:Th (pmol:dpm), 100–400 m	18 (14)	11	5–45	9 (10)	16	3–41	2 (1)	36	1–6
Co:Th (pmol:dpm), 0–100 m	19 (21)	16	1–78	8 (4)	9	2–13	2 (1)	29	1–5
Co:Th (pmol:dpm), 100–400 m	7 (4)	11	3–15	3 (1)	16	2–6	5 (6)	35	1–23
Mn:Th (pmol:dpm), 0–100 m	480 (730)	16	20–2800	120 (90)	9	30–280	50 (20)	29	20–110
Mn:Th (pmol:dpm), 100–400 m	100 (80)	11	30–270	120 (140)	16	20–590	530 (460)	36	30–1800

Note. POC = particulate organic carbon; SD = standard deviations; SEM = standard errors.

The profile patterns of Cd_{LP}:Th_{LP} in the Shelf and Offshore closely paralleled the surface to 400-m decreases (and occasional subsurface maxima; Figure S3) observed for P_{LP}:Th_{LP}. The zonal means for Cd_{LP}:Th_{LP} and P_{LP}:Th_{LP} were similar, albeit 3 orders of magnitude apart (Table 2). Like P_{LP}:Th_{LP}, Cd_{LP}:Th_{LP} had a large range in the upper 100 m (2–560 pmol/dpm). Interestingly, at most Gyre stations, Cd_{LP}:Th_{LP} increased with depth below 150 m and this was not observed with P_{LP}:Th_{LP}. This slight increase, however, did not change the overall pattern of decreasing P_{LP}:Th_{LP} between the surface and 400 m.

Co_{LP}:Th_{LP} zonal means were similar across the transect even though ratios decreased with depth in the Shelf and Offshore and increased in the Gyre (Table 2). The zonal means, regardless of depth range, were all between 2 and 8 pmol/dpm, except for 0–100 m in the Shelf (19 pmol/dpm). In the Gyre, the mean Co_{LP}:Th_{LP} increased from 2 pmol/dpm (0–100 m) to 5 pmol/dpm (100–400 m) and the range in values observed 100–400 m was larger than in the upper 100 m.

The Mn_{LP}:Th_{LP} profiles in the Shelf and Offshore generally followed the patterns observed in the Mn_{LP} concentration profiles, decreasing with depth in the shelf and offshore and increasing with depth in the Gyre (Table 2). Mn_{LP}:Th_{LP} across the transect ranged from 20 to 2,800 pmol/dpm. The upper 100 m in Shelf (480 ± 730 pmol/dpm) and the 100–400-m depth region in the Gyre (530 ± 460 pmol/dpm) had almost identical means, albeit with large standard deviations, which was unique to Mn. The remaining four depth regions all had means that fell between 50 and 120 pmol/dpm. Mn_{LP}:Th_{LP} began to increase with depth in the Gyre at around 100-m depth, shallower than observed for Co:^{234}Th.

3.3. ^{234}Th-Derived Particulate Fluxes

We have assessed the longitudinal changes in export for each component with respect to the three major transect zones (Figure 1) and report the zonal means with both standard deviations (SD) and standard errors (SEM = SD/$\sqrt{n}$; Table 1). The relative uncertainty on individual station fluxes used to calculate the zonal means was small compared to the relative SD of the zonal means (see Tables S1–S6 for individual station data). For example, the average relative uncertainty on individual Mn fluxes in the Shelf was 27% at 100 m, while the mean flux was 1,000 nmol·m^{-2}·day^{-1} with a relative SD of 120%. The fluxes of Mn had the highest individual station uncertainties of all the components by far, with an average relative uncertainty for 100- and 200-m fluxes of 29% (range 10 to 67%). The SEM better reflected the uncertainty on the individual station measurements going into the zonal averages than the SD; however, the large relative SD, especially for Cd and Mn in the Shelf, indicated that intrazonal variability was high for these components. A single order of magnitude higher Cd and Mn flux skewed the Shelf zonal means (n = 5). This suggested that the distribution of Shelf data was not normal for these two components and additional stations would be helpful in further assessing the mean flux for this zone. We focus our comparisons on the zonal means to highlight the large-scale differences in particulate cycling of these components across the southeastern Pacific and the SEM and SD should be considered in tandem.

The ratio of the particulate flux of a given component between two depth horizons was also assessed to characterize how the sinking flux might be altered. In this study, the flux ratio has been calculated by dividing the flux of a component at 200 m by the flux at 100 m (Table 1). As noted earlier, winter mixed layers do not generally reach deeper than 100 m (Fiedler & Talley, 2006) and the deepest E_z depths are slightly under 200 m. For a strictly biological component like POC, the flux ratio is the carbon transfer efficiency over this 100-m depth zone (Buesseler & Boyd, 2009). For components like Mn, whose export can be impacted by additional processes, such as scavenging, in situ precipitation, and dissolution, the flux ratio was used as an indicator of whether there had been a loss from the sinking particle pool (flux ratio < 1) or an increase in particulate flux (flux ratio > 1) between these two depths.

3.3.1. Particulate Fluxes and Flux Ratios

Locations along the transect had relatively similar ^{234}Th fluxes at 100 m, except the coastal stations from 77°W to 84°W, whose ^{234}Th flux estimates were adjusted for the impact of upwelling (Black et al., 2018). Stations west of 85°W had ^{234}Th fluxes at 100 m ranging between 1,100 and 2,000 dpm·m^{-2}·day^{-1}, while the Shelf had an average flux of 6,500 dpm·m^{-2}·day^{-1}. Most stations across the transect had a decrease in ^{234}Th flux through the 100- to 200-m zone. Because of the relatively small differences observed in ^{234}Th fluxes within a given zone, the $Comp_{LP}$:Th_{LP} became the most important factor governing the export of each component.

As expected, POC export decreased with depth and there was a decrease across the transect, with the largest 100-m flux at the coast and the smallest at the westernmost station (Figures 1 and 2). The average POC flux at 100 m ranged from 9 mmol·m^{-2}·day^{-1} in the Shelf to 1.6 mmol·m^{-2}·day^{-1} in the Gyre, with relative SD $\leq$ 50% (Table 1). For individual station data, relative uncertainties were below 18%. The average flux ratio for POC in the Shelf was higher than in the other two zones and ~1, suggesting that there was no net attenuation of POC (Table 1). In the Offshore and Gyre, all the flux ratios for POC were below 1, with zonal means of 0.5 and 0.7, respectively, and a range of 0.1–0.9. In summary, there was substantial POC remineralization below the E_z and the Offshore had a lower mean flux ratio than the Gyre.

Generally, the export of P decreased with depth and across the transect (Figures 1 and 2) The largest flux at 100 m (900 μmol·m^{-2}·day^{-1}) was observed in the Shelf and the smallest was at the westernmost station (8.2 μmol·m^{-2}·day^{-1}; Figure 1). A ninefold decrease was observed between the mean Shelf P flux at 100 m (~300 μmol·m^{-2}·day^{-1}) and the mean for the Offshore (33 μmol·m^{-2}·day^{-1}), reflecting the large gradient in P_{LP}:Th_{LP} observed (Tables 1 and 2). Particulate Cd fluxes decreased sevenfold between the two zones, while the remaining components had a threefold to fourfold change. The flux ratios for P were almost always $<$1 (0–1.3; Table 1), reflecting that remineralization was the dominant process affecting particulate P in the upper 200 m. Occasional subsurface peaks, like at stations 11 and 18 (94°W and 112.8°W), led to local flux ratios that were over 1. These were also observed with Cd.

Cd export and flux ratios followed the same depth and across-transect patterns observed for particulate P (Figures 1 and 2), although the relative magnitude of flux change over a given depth interval was occasionally different for Cd and P. For instance, at 112.8°W, particulate Cd fluxes followed the depth increases of particulate Co and Mn more closely. Cd export at 100 m ranged from 2.1 nmol·m^{-2}·day^{-1} (132.5°W) to 1,000 nmol·m^{-2}·day^{-1} (79.2°W). The variability in Cd export and flux ratios in the Shelf was the largest relative to all other components (Table 1).

Co export across the transect ranged from 1 to 70 nmol·m^{-2}·day^{-1}, with the zonal means varying by an order of magnitude from the Shelf to the Gyre (Table 1). Particulate Co fluxes decreased with depth from the coast until 100°W, where the subsurface ODZ was still present (Table 1 and Figure 2). Offshore flux ratios ranged from 0.1 to 0.7, indicating that remineralization was dominant here. In the Gyre, the range in Co flux ratios was 0.1 to 2.1 and the mean was 1.3 ± 0.2. Although the average Co flux at 100 m in the Gyre did not differ from the 200-m mean (3.3 nmol·m^{-2}·day^{-1}), 8 of 12 stations had a larger flux at 200 m, reflecting a real increase with depth. These results reflected the start of the shift in the processes governing the distributions of particulate Co fluxes with depth in the Gyre. Although remineralization was occurring between 100 and 200 m, as indicated by decreasing POC fluxes, the cumulative impact of all processes, including precipitation and scavenging, produced a net addition of Co to the sinking pool at many of the stations.

The export of Mn at 100 m did not precipitously decrease from the shelf to the gyre like the drop in flux that was seen for particulate P, Cd, and Co (Figures 1 and 2 and Table 1). Nevertheless, there was still a sevenfold

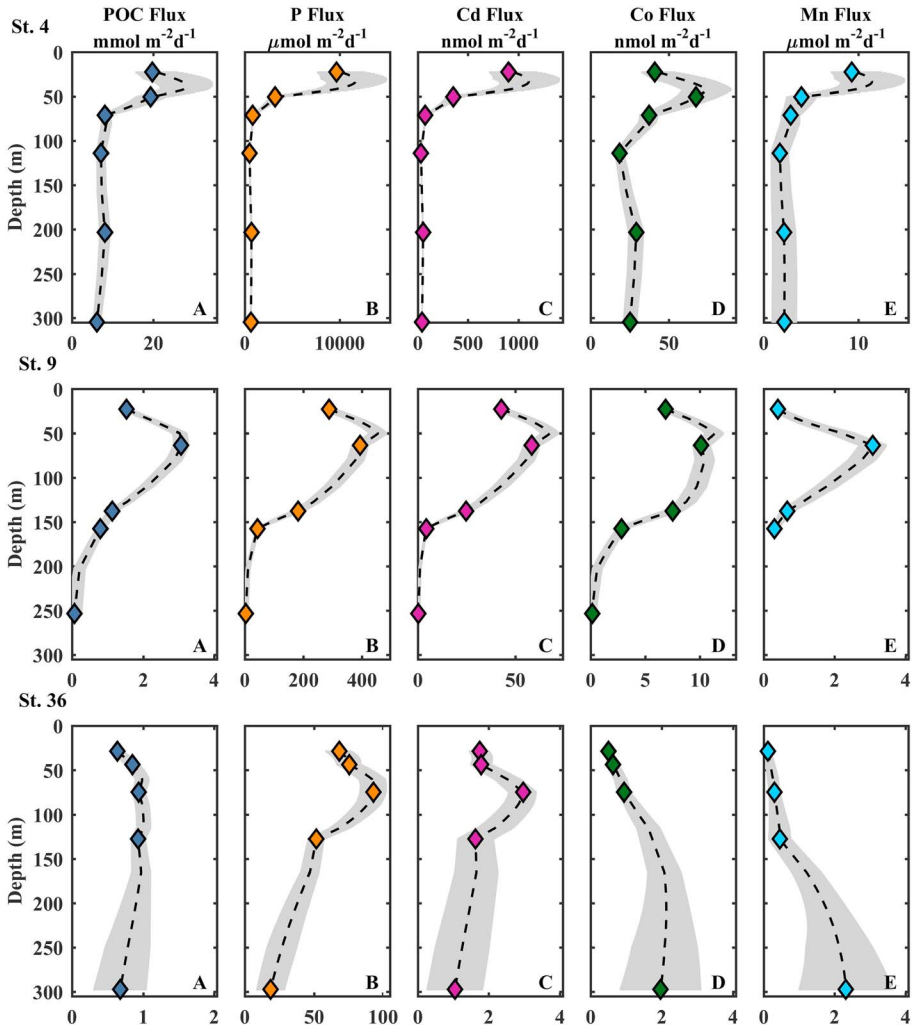

Figure 2. Particulate fluxes for characteristic Shelf (Station 4), Offshore (Station 9), and Gyre (Station 36) stations. (a–e) The fluxes for POC, P, Cd, Co, and Mn, respectively. Fluxes were calculated by multiplying the ^{234}Th flux by the large particle Comp:Th at the depth of Comp:Th sampling (diamonds). Dashed lines show interpolated fluxes. Note that total ^{234}Th measurements (and by extension ^{234}Th fluxes) were taken at a greater number of depths than Comp:Th. Errors are indicated by gray shading. To see a visual progression from ^{234}Th flux and Comp:Th to particulate flux profiles, refer to Figures S4–S6 and for individual station data, see Tables S1–S6. POC = particulate organic carbon.

difference in the mean at 100 m between the Shelf and Gyre. Particulate fluxes across the uODZ were assessed for Mn because of its redox sensitivity (see Table S5 for individual station flux across the uODZ). East of 100°W, Mn fluxes increased from the surface until the uODZ and below the uODZ the fluxes dropped significantly. All eight of the shelf and offshore stations that had quantifiable Mn flux values at the uODZ and uODZ + 100 showed a sharp decline in flux over this 100-m layer, which was also reflected in the flux ratios from 0.1 to 0.8 and suggested that Mn was lost from the large particle pool. Above the uODZ, Mn(III–IV) oxyhydroxides precipitated, and below the uODZ, these particulate phases were reductively dissolved (Ohnemus et al., 2016). In the Gyre, the average Mn flux ratio increased to 4.9 ± 0.4 (Table 1) and ratios ranged from 3.0 to 8.0. All flux ratios in the Gyre were a result of an increase in Mn in the large particle pool.

3.3.2. Bio-Authigenic and Lithogenic Fractions of Export Fluxes

P_{LP} and Cd_{LP} concentrations at 100 m, and therefore particulate P and Cd fluxes, were ≤1% lithogenic at all stations (Table 1). The lithogenic fraction of the Co flux at 100 m rose to 18% near the coast, with a mean Shelf value of 9%. Conversely, the 100-m fluxes at the Offshore and Gyre stations were ≥98% bio-authigenic. Overall, the percent lithogenic fraction from 100 to 200 m did not change for these three components,

although the Co flux was slightly more lithogenic at 200 m, on average, and one relatively high 200-m value was observed for Cd and P at 99°W (~30%). Mn fluxes, on the other hand, had an average lithogenic component >50% in the Shelf at 100 m, with Mn_{LP} most likely originating from local dust sources or coastal shelf fluxes (Table 1). The average lithogenic fraction of the Mn flux at 100 m was much lower for the Offshore (4%) and Gyre (2%).

3.4. Residence Times

Zonal averages for τ_{LP} in the upper 100 m were between 4 and 19 days for all components and the vast majority of τ_{LP} for all individual stations were between 0.5 and 26 days. The mean τ_{LP} for each zone was similar for POC, P, Cd, and Co (Table 1). For each of these components, the mean τ_{LP} in the Shelf was the lowest of the three zones (5–10 days) and the Offshore the highest (13–16 days). In the Gyre, τ_{LP} ranged from 9 to 12 days. P and Cd had marginally longer τ_{LP} than POC and Co in all zones. Mn, on the other hand, had shorter mean τ_{LP} in the Offshore and Gyre and Mn τ_{LP} values were the same in the upper 100 m of the Shelf and Offshore.

The τ_{Tot} for the upper 100 m were generally on the order of years and were much longer than the τ_{LP} due to the large dissolved inventories of most components (Table 1). For all stations, the τ_{Tot} of Cd, Mn, and Co ranged from 0.1 to 5.1 years and the τ_{Tot} for P from 0.5 to 12.9 years. For P, Co, and Mn, the τ_{Tot} mean was longest in the Offshore and for Cd, the longest was the Shelf.

The average 0–200 m τ_{Tot} were also determined for the TM in each zone (Figure 3). These τ_{Tot} were longer than the τ_{Tot} for 0–100 m (>3 years), except Mn which had a shorter average τ_{Tot} of 0.9 years in the Gyre. All three TM had τ_{Tot} > 10 years for 0–200 m in the Offshore. The τ_{Tot} for station 9 (89°W) were anomalously high (Cd = 227 years, Co = 91 years) compared to the mean τ_{Tot} for this depth zone using the other three Offshore stations (Cd = 12 years, Co = 10 years). The longer τ_{Tot} at station 9 can be attributed to a significantly lower flux (flux ratios 0.03–0.07) and equal or greater inventories relative to those of the surrounding stations. The particulate flux of Mn was within the method uncertainty (10 ± 10 nmol·m^{-2}·day^{-1}) at station 9 and the 0–200 m Mn τ_{Tot} for the Offshore excludes this station (Figure 3).

4. Discussion

4.1. ^{234}Th Variability

^{234}Th production by ^{238}U and its short half-life limit the possible activities of ^{234}Th in the surface ocean. $^{234}Th_{LP}$ activities in the upper 400 m ranged from 0.01 to 0.4 dpm/L (mean = 0.1 dpm/L), which amounted to <1–22% of total ^{234}Th. This was approximately threefold higher than the range (0.005–0.08 dpm/L) and mean (0.03 dpm/L) observed during the Atlantic GA03 campaign (Owens et al., 2015). Although interbasin differences exist and seasonal changes will impact intrabasin variability, the range in total ^{234}Th values is small compared to the orders of magnitude variations in particulate TM concentrations observed here. This suggests that ^{234}Th activities are not the predominant source of variability in Comp:Th ratios and the subsequent flux calculations.

4.2. Zonal Patterns in Large Particle Concentrations

Until the start of the GEOTRACES program, size-fractionated particulate measurements of TM were rare (e.g., Bishop et al., 1977; Frew et al., 2006; Weinstein & Moran, 2004) and often limited to a select few metals (e.g., Bishop & Fleisher, 1987; Lam et al., 2006) or a single location (e.g., Cullen & Sherrell, 1999). Methodological differences, such as the filter pore size considered for "sinking" particles, can further complicate historical comparisons; however, prior studies will be referenced, when possible, to put this study's results in a global context.

POC_{LP} (0 to 1.5 μM; Lam et al., 2015), P_{LP} (0 to ~40 nM; Twining et al., 2015), Cd_{LP} (0 to 8 pM; Twining et al., 2015), and Co_{LP} (0 to 5 pM; Twining et al., 2015) measured in the upper 400 m in the North Atlantic were similar in magnitude to the results from this transect. On the other hand, the range observed for Mn_{LP} was much smaller than observed elsewhere. Mn_{LP} in the upper ocean in the North Atlantic can exceed 1,000 pM (Bishop & Fleisher, 1987; Twining et al., 2015), much larger than observed here (maximum = 150 pM). This Mn_{LP} difference is present despite the similarity in surface Mn_{Diss} that were measured along both the North Atlantic and Pacific campaigns (Hatta et al., 2015; Resing et al., 2015). This

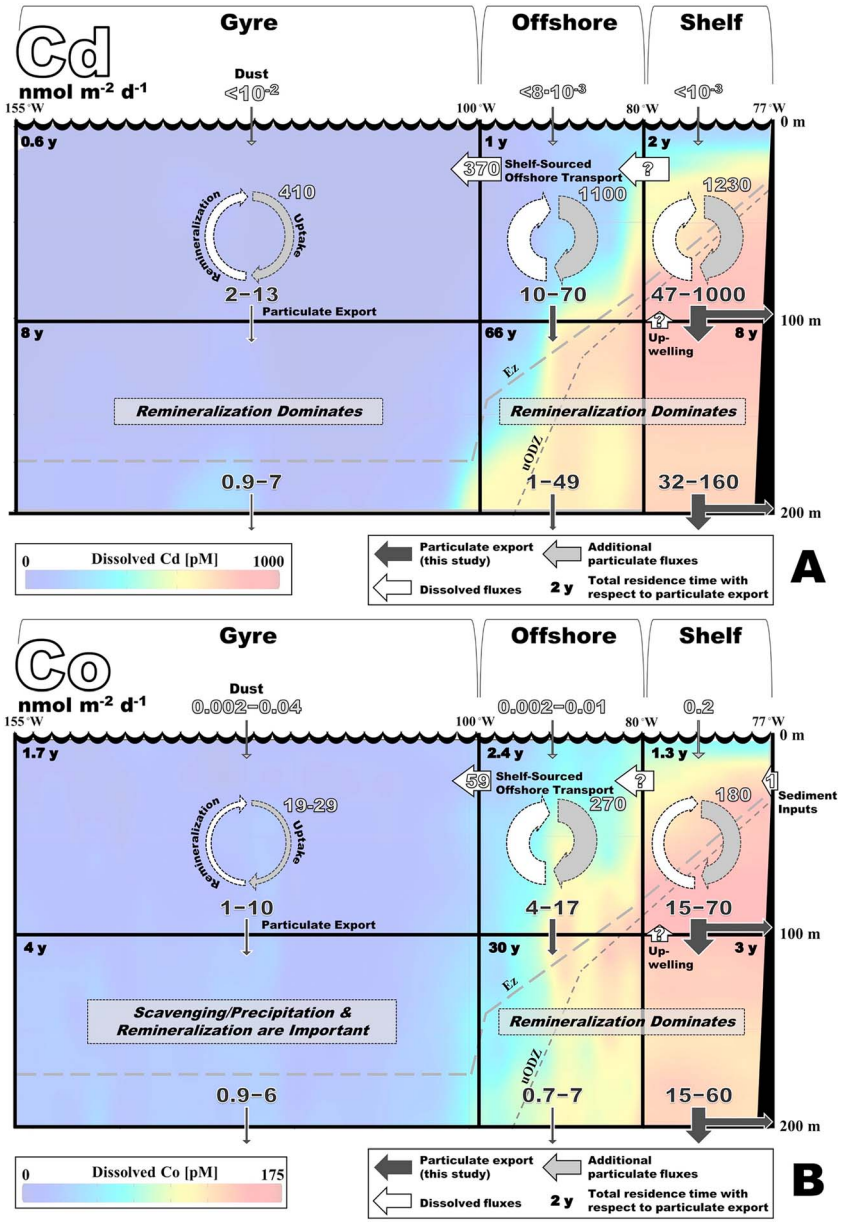

Figure 3. Particulate cycling of (a) Cd, (b) Co, and (c) Mn in the southeastern tropical Pacific. The range in particulate export is shown with estimates of uptake and dust flux ranges for each zone. Uptake was determined by multiplying Moderate Resolution Imaging Spectroradiometer-derived averages of net primary production by the estimated TM:C in bulk phytoplankton. Net primary production values were 114, 99, and 96 mmol C m^{-2} day^{-1} for the Shelf, Offshore, and Gyre, respectively (Black et al., 2018). Co:P and Cd:P were measured on bulk particulate matter (>0.45 μm) within the mixed layer of the Shelf and Offshore stations (Ohnemus et al., 2016). A bulk particle C:P of ~50 mol/mol for these zones was used to determine the corresponding Co:C and Cd:C ratios needed to determine Co_{Diss} and Cd_{Diss} uptake (Lam et al., 2018). Mn:C and Co:C from bulk particle analyses in the equatorial Pacific (20–25 m; Twining et al., 2011) were used to estimate Mn_{Diss} uptake for all zones and Co_{Diss} uptake in the Gyre. Potential pathways for the advection of dissolved constituents are indicated with magnitudes when known, including offshore transport (Sanial et al., 2018), and sediment fluxes of Mn (Scholz et al., 2011) and Co (Hawco et al., 2018). All fluxes are reported in nanomoles per square meter per day. Total residence times (τ_{Tot}; upper left corners of each zone) in years are reported for depth intervals of 0–100 and 0–200 m.

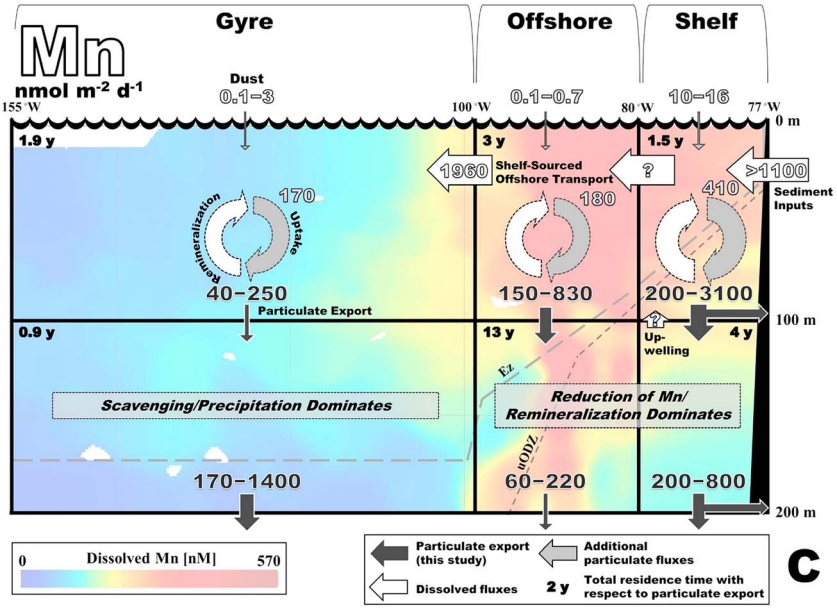

Figure 3. (continued)

difference might be attributed to a combination of the larger Mn inputs from dust and rivers in the Atlantic versus the Pacific (van Hulten et al., 2017), differing characteristics of coastal waters in the two basins (e.g., higher concentrations of humics in the North Atlantic promoting oxidation), and the reduction of Mn within the ODZ at the coastal Pacific stations.

POC_{LP}, P_{LP}, and Cd_{LP} profiles in all three zones reflect the production of organic matter in the sunlit upper ocean and remineralization of these constituents as particles sink. POC and P are useful biological endmembers because they are almost exclusively associated with biological matter in the upper ocean and the relationships of POC, PON, and particulate P on this transect matched the general stoichiometry of plankton (Lam et al., 2018). The elevated levels of P_{LP}, Cd_{LP}, and Co_{LP} near the uODZ have been shown to be in excess of those that would be expected as a result of Fe oxyhydroxide scavenging, suggesting luxury uptake by local phytoplankton communities (Lee et al., 2018; Ohnemus et al., 2016). Cd_{LP} profiles mirrored those of P_{LP}. The steeper decline in P_{LP} and Cd_{LP} with depth compared to POC_{LP} reflects a shorter remineralization length scale for P and Cd (Lam et al., 2018).

Co_{LP} and Mn_{LP} had different profile patterns than POC_{LP} or P_{LP}. Co_{LP} profiles followed the pattern of POC in all regions except below 150 m in the Gyre. The increase in Co_{LP} here could result from scavenging onto large particles as a result of the co-oxidation of Co and Mn (Moffett & Ho, 1996) or the aggregation of smaller particles (Lam et al., 2018). Mn_{LP} decreased with depth at stations east of 99°W, where redox conditions below the uODZ led to the substantial decline in particulate Mn, and increased with depth in the Gyre, where Mn oxyhydroxides were able to form with no ODZ. While this precipitation can be attributed to Mn-oxidizing bacteria (as can the coprecipitation of Co), the resulting particulate concentration profiles do not follow the typical pattern of a biologically utilized nutrient, which generally has the highest particulate concentrations at the surface.

4.3. Zonal Patterns in Large Particle Ratios

For the nutrient-like components, the most variability in Comp:Th was observed in the upper 100 m of the Shelf and POC had the smallest relative SD (Table 2). In general, POC and P had the least Comp:Th variability with depth and smallest Comp:Th ranges at depth (100–400 m). Co_{LP}:Th_{LP} and Cd_{LP}:Th_{LP} showed less consistency, especially in the Gyre where Comp:Th tended to increase for both components in the 100- to 400-m depth range. Of the TM assessed here, only Cd has any published Comp:Th (Smith et al., 2014) and these values for the Scotian Shelf and Gulf of Maine ranged from <1 to 350 pmol/dpm.

The shape of the Mn_{LP}:Th_{LP} profiles in the Shelf and Offshore, like the Mn_{LP} profiles, suggests an increased presence of Mn-oxidizing bacteria in low-light surface waters (increasing particulate Mn_{LP}:Th_{LP} with depth) and reflects the change in redox conditions at the uODZ (decreasing in particulate Mn_{LP}:Th_{LP}). Mn_{LP}:Th_{LP} in the Gyre increased with depth, suggesting that the scavenging mechanisms increasing Co_{LP} (and potentially Cd_{LP}) could be related to the increase and/or scavenging of Mn. Compared to the mean 0–100 m Mn_{LP}:Th_{LP} in the Gyre, the 100- to 400-m mean was fivefold larger, consistent with photoinhibition and/or photoreduction in the surface or the precipitation of Mn oxides and the influence of Mn-oxidizing bacterial processes between 100 and 400 m (Table 2).

Although mixed layer POC_{LP}:Th_{LP} have been shown to vary substantially (Buesseler et al., 2009; Passow et al., 2006), this Pacific campaign and the Atlantic GEOTRACES cruises illustrate that subsurface POC_{LP}:Th_{LP} ratios in ocean gyres seem to converge into a relatively small range (Black et al., 2018; Owens et al., 2015). For example, in the North and South Atlantic gyres, ratios approached a value of 2 μmol/dpm at 200 m and here in the Gyre ratios averaged 0.7 ± 0.1 μmol/dpm (E_z to 400 m). This suggests that for components that behave like POC, it might be possible to sample at fewer locations or subsurface depths to define Comp:Th in a given region. Conversely, given the higher variability for the other Comp:Th, whether across the entire transect or in a single region (e.g., Cd in the Gyre), there is a need for high-resolution sampling until this variability can be understood.

4.4. On the Use of Small and Large Particle Components to ^{234}Th Ratios

Differences between the large and small particle Comp:Th ratios could impact export estimates if the small particle pool contributes substantially to the sinking particle flux. While recent sediment trap work has suggested that smaller, presumably slower sinking particles contribute to the overall export in oligotrophic regions (Durkin et al., 2015; Hung et al., 2012; Puigcorbé et al., 2015), it is unclear if smaller particles caught in traps are transported as large fast sinking particles that disaggregate at depth or if they arrive as single small particles. If the former is the case, then the large particle ratio is still the most appropriate when using the ^{234}Th approach. A study in the northwestern Pacific also showed elevated Mn in subsurface traps that could be attributed to small, slow sinking Mn-rich particles that originate from large lateral shelf plumes (Lam & Bishop, 2008; Lamborg et al., 2008). Further study in a variety of biogeochemical regions is necessary to determine (1) whether the small particles play a substantial role in the total regional export for a give site and season, (2) whether small particles are sinking fast enough to contribute to the export, and (3) whether the large- and small particle Comp:Th ratios differ enough that varying contributions of each could change the total export derived from ^{234}Th. These questions could be addressed by a sampling campaign employing both trap and ^{234}Th methods. Here we can only compare the Comp:Th for both size fractions to see if there are differences.

Plotting the large particle Comp:Th versus the small particle Comp:Th demonstrates the potential impact (if any) that using various combinations of the ratios could have on the flux of each component (Figure S7). Because the 100- and 200-m data for POC, P, Cd, and Co generally fall about the 1:1 line for this study, using the large or small particle Comp:Th would produce the same export estimates. On the other hand, the ratios for Mn lie closer to a 1:2 line, where the Mn_{SP}:Th_{SP} ratios are 50% smaller than the Mn_{LP}:Th_{LP}. This ratio difference would be important if the small particles were a substantial contributor to the total flux. Furthermore, the coefficients of determination (r-squared) for linear regressions of $Comp_{LP}$:Th_{LP} versus $Comp_{SP}$:Th_{SP} for all sampling depths 0–200 m (n = 85 to 88) are 0.85 for POC, and ranging from 0.52 to 0.65 for the remaining components ($p \ll 0.05$). The lowest r-squared correspond to the Co and Mn regressions. The smaller scatter in the POC ratio data suggests a tighter coupling of the processes impacting the small and large size particles (e.g., production of small particles and aggregation to large particles), whereas the larger scatter with the Co and Mn ratio data indicates that there are other processes that are affecting the small and large particles independently.

4.5. Controls on the Distribution of Particulate Fluxes

Although all of the components had a decreasing gradient in export from the Shelf to the Gyre, this pattern was most consistent for Cd, P, and Co (Figure 1), suggesting that similar processes were impacting the particulate flux of these components in the upper 100 m. Particulate Cd, P, and Co fluxes show, on average, a 54-, 18-, and 12-fold decrease, respectively, between the Shelf and the Gyre, while POC fluxes show only

sixfold decrease (Table 1). The decrease in POC export parallels a decrease in satellite-based net primary production (NPP) of 188 to 34 mmol C·m^{-2}·day^{-1} from the coast to 152°W (sixfold change; Black et al., 2018). While it is evident that production and remineralization are governing the distribution of the biologically relevant components, these differences suggest that the processes that control the removal of POC from the large particle pool are perhaps more variable and/or intense for particulate P, Cd, and Co. In addition, these gradients in export could partly reflect differences in Comp:Th caused by variations in cell quotas and uptake in a given zone, which could differ for P, Cd, and Co with respect to a similar C demand (Martiny et al., 2013; Twining & Baines, 2013). Although the average Mn export at 100 m for the Shelf and Gyre reflects a similar sixfold difference to those of POC, the gradual decline of particulate Mn fluxes in the Offshore and Gyre and the lower relative SD in these zones is a result of a tight balance between processes resulting in Mn oxide dissolution in the sunlit upper ocean and oxidation by bacteria in the subsurface, not one of production and remineralization.

The flux ratios for POC, P, and Cd in all zones clearly reflect remineralization (Table 1), while Co and Mn flux ratios greater than 1 indicate the influence of additional processes. Without in situ, incubation-based uptake rates for P and Cd, the absolute percentage of surface production reaching depth cannot be calculated, but production and remineralization undoubtedly dominate processes governing their particulate flux distributions. Mn flux profiles in the Gyre, on the other hand, show the greatest increases with depth seen across the transect and the largest number of flux ratios >1. The large shift in flux ratios between the Offshore and the Gyre suggests that Mn is uniquely impacted by redox conditions in the ODZs, which lead to a decrease in export with depth, and scavenging and/or precipitation in the Gyre, which increases Mn flux with depth. While the Co flux ratios for the Shelf and Offshore closely match those of POC, the flux ratios of Co in the Gyre more closely matched those of Mn. Greater than 75% of the Co flux ratios are at or above 1 in the Gyre, suggesting that Co export increases with depth at individual stations within this zone. Therefore, the distribution of Co_{LP} and the flux of Co reflect two region patterns. In the low-oxygen regions, the pattern is mostly biological, where Mn oxidation cannot occur (preventing any co-oxidation of Co and subsequent increase in particulate Co). In the Gyre, the pattern reflects scavenging below 100 m in the Gyre.

Only one prior study simultaneously sampled total ^{234}Th and TM_{LP}:Th_{LP} ratios (Cd; Smith et al., 2014). Comparison to this study and those utilizing traps is complicated by collection differences, including the deployment depths and season sampled, which we know from prior studies may be responsible for some of the observed variability. The Offshore and Gyre export of P at 100 and 200 m (1.3–57 μmol·m^{-2}·day^{-1}) are slightly higher than those observed in the North Atlantic gyre using traps at 150 m (0.95–4.7 μmol·m^{-2}·day^{-1}; Stanley et al., 2004) and the Shelf P export (46–900 μmol·m^{-2}·day^{-1}) are much lower than 150-m trap fluxes observed in the Benguela upwelling region (800–2,300 μmol·m^{-2}·day^{-1}; Noble et al., 2012). ^{234}Th-based Cd export estimates from the western North Atlantic are relatively similar at 50 m (1–31 nmol·m^{-2}·day^{-1}) to those of the Offshore and Gyre regions (Smith et al., 2014). Shelf Cd export in the Shelf, ranging from 47 to 1,000 nmol·m^{-2}·day^{-1}, is high compared to all other previous studies using traps or ^{234}Th (Migon et al., 2002; Pohl et al., 2004; Schüßler et al., 1997). Co export from a study using estimated Co_{LP}:Th_{LP} ratios from the western Atlantic (Dulaquais et al., 2014), traps from the Benguela upwelling region, and traps from the northwestern Pacific (Lamborg et al., 2008) all fall in between 2 and 30 nmol·m^{-2}·day^{-1}. These Co flux ranges are close to those found on this transect at 100 and 200 m (0.7–70 nmol·m^{-2}·day^{-1}).

The results from this study can be compared to numerous other Mn export studies (upper 400 m), although all have used sediment traps (e.g., Lamborg et al., 2008; Martin & Knauer, 1983). Excluding the outlier from station 1 (3,100 nmol·m^{-2}·day^{-1}), the range in particulate Mn fluxes observed in this study at 100-m depth is 40–830 nmol·m^{-2}·day^{-1} and 60–1,400 nmol·m^{-2}·day^{-1} at 200-m depth. These ranges are larger than those observed in most other basins that have been studied, but similar fluxes (20–5,000 nmol·m^{-2}·day^{-1}) were found in the low-oxygen regions off California and Mexico (Landing & Bruland, 1987; Martin et al., 1985, 1980; Martin & Knauer, 1983, 1984). In other open ocean regions, export ranged from 10 to 280 nmol·m^{-2}·day^{-1}, with the highest fluxes observed in the waters east of New Zealand and in the North-East Water Polynya (Ellwood et al., 2014; Schüßler et al., 1997) and the lowest in the Benguela upwelling region (Noble et al., 2012). No upper ocean estimates from Indian and Southern Oceans are currently available for comparison (Figure S1).

4.6. Sources, Sinks, and Internal Cycling of Particulate TM

To better understand the controls on the upper ocean export of TM, the magnitude of surface inputs and the time scales of removal for each component must be considered. Summary schematics (Figure 3), incorporating results from this study, cell ratio- and NPP-derived uptake estimates, dust fluxes, and ^{228}Ra-based offshore transport estimates for dissolved constituents (Sanial et al., 2018), help illustrate the relative magnitude of processes impacting particulate budgets in the upper 200 m. Ranges in bulk dust fluxes to the surface were derived for each zone using dust-model estimates for each station within a zone (approximately 1 month prior to sampling; Albani et al., 2014) and upper crust ratios for each element (Taylor & McLennan, 1995). ^{228}Ra-derived estimates represent the TM_{Diss} fluxes that originated from the shelf and are moving westward between the Offshore and Gyre. This shelf-sourced flux could originate from a combination of riverine, sediment, and subterranean groundwater inputs.

4.6.1. Particulate Cd Cycling

The decrease in particulate Cd fluxes with depth in the upper 200 m reflects the dominance of remineralization processes, with the greatest attenuation of Cd export in the Shelf and smallest in the Gyre (Figure 3a). Cd export from the upper 100 m could represent $<$5% of the Cd_{Diss} taken up by surface plankton in the Offshore and Gyre and almost 25% in the Shelf. This pattern is similar to that seen for POC export (Black et al., 2018); in that, the absolute magnitude of Cd export is largest nearer to the coast due to high surface productivity, although flux attenuation for POC is greatest in the Shelf and Offshore.

The uptake of Cd_{Diss} by surface communities and the subsequent sinking of this organic material is the most likely source of the export of Cd because the bio-authigenic fraction of Cd export at 100 m was $\geq$99% at all stations. Furthermore, dust estimates for this region are $<$0.01 nmol·m^{-2}·day^{-1} or 0.5% of the smallest 100-m particulate Cd flux observed here, confirming that aerosol sources are negligible. The sediments in this region are unlikely to be a significant source of Cd_{Diss} (Janssen et al., 2014; Rosenthal et al., 1995). The Ra-derived estimate for the transport of Cd_{Diss} from the coastal region is similar to the uptake rate for the Gyre and much larger than the observed export, suggesting that the supply of Cd_{Diss} from the coast would be enough to support surface communities in the Gyre and that Cd should not be a major limiting factor of productivity in the region.

4.6.2. Particulate Co Cycling

Co export decreases from 100 to 200 m due to remineralization in the Shelf and Offshore, similar to Cd export (Figure 3b). The particulate flux of both decrease by ~60% from 100 to 200 m in the Offshore, while Co export in the Shelf shows surprisingly little attenuation relative to that seen for Cd. The uptake estimates for this transect (19–270 nmol·m^{-2}·day^{-1}) are comparable to those determined for the Atlantic and Southern Oceans (7–220 nmol·m^{-2}·day^{-1}; Bown et al., 2011; Dulaquais et al., 2014). In the upper 100 m, the export of Co is 22%, 4%, and 10% of the surface uptake in the Shelf, Offshore, and Gyre, respectively. The export percentage in the Gyre is similar to the 18% determined at 100 m at the Bermuda Atlantic Time Series station in the Atlantic (Dulaquais et al., 2014). The larger degree of attenuation of particulate Co in the Offshore was anticipated due to the high attenuation of POC; however, more Co is exported in the Gyre (10% of surface uptake) relative to Cd (1%). The scavenging of Co could contribute to the higher relative export of Co in the Gyre, and the increase in particulate Co fluxes (100 to 200 m) at 8 of 12 stations suggests a slight switch from a remineralization-dominated system to one controlled by scavenging and/or coprecipitation. While some degree of Co scavenging in the Offshore and Gyre is possible, it is likely slower or unfavorable in the ODZ due to the reduction of particulate Mn.

The lithogenic fraction of the Co export at 100 m ranges between 1% and 19% in the Shelf but averages only 1% in the Offshore and Gyre, suggesting that particulate inputs from dust and sediments are relatively small in this region. The dust input to the Gyre ranges from 0.004 to 0.01 nmol·m^{-2}·day^{-1} which is, at most, 0.8% of export if the station with the lowest particulate Co flux is used. Therefore, long-term sources of the dissolved Co pool in the Gyre most likely originate from coastal fluxes and upwelling, which is consistent with recent global modeling results (Hawco et al., 2016; Saito et al., 2004; Sanial et al., 2018; Tagliabue et al., 2018). Ra-based estimates suggest that 59 nmol Co·m^{-2}·day^{-1} is being supplied from the shelf to the gyre (Sanial et al., 2018). This offshore transport of Co_{Diss} could provide enough Co_{Diss} to supply the uptake in the Gyre and the export observed at both 100 and 200 m.

4.6.3. Particulate Mn Cycling

The uptake-export relationship for Mn is distinct from the other components assessed here. For Cd and Co, the estimated uptake is always much greater than the export at 100 or 200 m because phytoplankton production dominates in the surface and remineralization rates govern the export below the E_z (Figures 3a and 3b). In contrast, Mn cycling is dominated by redox cycling between a particulate oxidized phase and a dissolved reduced phase, which is in turn controlled by light and the redox potential of the water column. In the euphotic zone, light inhibition of Mn oxide precipitation (Francis et al., 2001) and photoreduction of Mn oxides (Sunda & Huntsman, 1994) prevents Mn oxide accumulation. In the ODZ, the low redox potential results in the reductive dissolution of Mn oxides. Precipitation of Mn oxides is therefore most important in a zone that is below the E_z but above the uODZ. This narrow depth range of Mn oxide precipitation is schematically indicated in Figure 3c, and occurs in the upper 100 m in the Shelf zone, and between 100 and 200 m in the Offshore zone. The ODZ does not extend laterally into the Gyre zone, so Mn oxide precipitation in the Gyre can occur anywhere below the E_z.

As a result of these processes occurring in different parts of the water column, the magnitude of the Mn export observed depends on the depth range of the Mn oxidation zone in each region relative to the 100- or 200-m export depths. For example, in both the Shelf and the Offshore zones, the Mn export at 100 m exceeds Mn uptake, reflecting the precipitation of Mn oxides above the 100-m depth horizon. Mn export decreases between 100 and 200 m, since the 200-m depth horizon is in the ODZ, where Mn oxides start to dissolve. In the Gyre, the Mn export at 100 m is of similar magnitude to Mn uptake, reflecting that 100 m is still in the euphotic zone where Mn oxide precipitation is low. If we assume that microbial Mn oxidation above the E_z is 0–2% of Mn_{Diss} per day (Moffett, 1990; Sunda & Huntsman, 1987) and an average Mn_{Diss} in the gyre (0–100 m) of 1 nM, the rate of oxidation removal could be between 0 and 2,000 nmol·m^{-2}·day^{-1}. At the maximum rate, only 8% of the oxidized Mn would need to sink to support the mean export of 160 nmol·m^{-2}·day^{-1} in the Gyre. Mn export increases almost fivefold from 100 to 200 m, since the 200-m horizon is well within the Mn oxide precipitation zone. Clearly, choice of depth horizon for assessing Mn flux must account for the euphotic zone depth and depth of ODZ, if present.

Mn export is relatively high despite the low dust flux to this region of the ocean (Figure 3c). In fact, Mn-specific dust estimates for the Pacific that are currently being employed in the first Mn OBGCM are as low as 20 nmol·m^{-2}·day^{-1} and the addition of sediment fluxes only increases the Mn sources in the region to 41 nmol·m^{-2}·day^{-1} (van Hulten et al., 2017). Although 53% of the Mn export at 100 m on the Shelf was characterized as lithogenic, dust inputs could not explain the large particulate Mn fluxes in the offshore and gyre where the composition at 100 m is 97% bio-authigenic. Furthermore, authigenic or scavenging processes are the most likely source because average Mn:P ratios (mmol/mol) at 100 m in the offshore and gyre are 12, much higher than the plankton ratios (0.35–0.53) previously observed in the equatorial Pacific (Twining & Baines, 2013). Ra-derived estimates for the offshore transport of Mn_{Diss} totaled 1,960 nmol·m^{-2}·day^{-1}, suggesting that Mn_{Diss} fluxes from the coastal shelf are much larger than predicted and would provide more than enough Mn to support the precipitation and/or scavenging leading to the observed Mn export. Not taking this offshore transport into account (and by extension larger Mn sources to the dissolved pool at the Shelf) may explain, in part, why the Mn OBGCM used by van Hulten et al. (2017) generally succeeded in reproducing global water column Mn_{Diss} distributions but was unable to match in situ Mn_{Diss} measurements in the Pacific OMZ. A single Mn_{Diss} flux from Peruvian Shelf sediments (85 m at 11°S, 77.8°W) was measured at 1,100 nmol·m^{-2}·day^{-1} (Scholz et al., 2011), which is only 56% of the estimated offshore flux of Mn_{Diss}. However, similar studies off the coast of California and on the Pakistan Margin have found larger sediment fluxes ranging from 6,600 to 11,000 nmol·m^{-2}·day^{-1} (Johnson et al., 1992; Law et al., 2009; McManus et al., 2012), suggesting that the sediments are the likely source for the Peruvian region's offshore transport of Mn_{Diss}.

4.7. Upper Ocean Removal Time Scales

The ^{234}Th-derived residence times for these components can provide insight into the processes controlling the distributions and particulate fluxes of TM in the surface ocean. The τ_{LP} expresses how rapidly the large particle pool is cycling and allows us to compare if the time scales of the processes impacting the large particle pools are similar for all components, including ^{234}Th. The total residence time τ_{Tot} (Figure 3) shows how quickly the particle flux is removing the surface inventory of each element or component.

4.7.1. Residence Times in the Upper Ocean Large Particle Pool

Most components have rapid τ_{LP} values on the order of a few days to weeks (Table 1). The shortest τ_{LP} values are generally found in the Shelf, although Cd has a large range in τ_{LP} values here. For the more nutrient-like components, τ_{LP} is rapid in the Shelf because export is large. Offshore τ_{LP} values are elevated above the other two zones because while export drops precipitously from the Shelf, large particle inventories for the upper 100 m are still relatively high in the Offshore. In the upper 100 m of the Offshore and Gyre, Mn has τ_{LP} averages that are at least half of the means for the rest of the components. All zonal τ_{LP} averages for Mn are six days or less, suggesting that the large particle pool of Mn cycles more rapidly than those of the other components and that Mn loss via the sinking of particles is relatively large compared to that of other components.

Not much data exist for a comparison of TM residence times within the large particle pool. However, a study of P cycling in the Gulf of Maine found that, while variable, the cycling of particulate P in the euphotic zone appeared to be on the order of days to just over a week in the coastal ocean (Benitez-Nelson & Buesseler, 1999). This range fits with the results from our study and support a relatively consistent time scale for large particle component cycling in the upper ocean. ^{234}Th, with a half-life of 24.1 days, is well suited for tracking components in the particulate phase over these time scales. Furthermore, if sinking rates are derived from the zonal τ_{LP} averages of each component (100 m divided by mean τ_{LP} at 100 m; Table 1), they fall within a range of 6–23 m/day, which is similar to the 7- to 25-m/day range from Dunne et al. (1997) for the equatorial Pacific.

4.7.2. Total Upper Ocean Residence Times With Respect to Export

The τ_{Tot} values for TM generally fall within other estimates for the global ocean utilizing non-^{234}Th-based methods (Table 1). Co τ_{Tot} for the upper 100 m in the Atlantic has been estimated between 0.32 years (particulate export-derived) to 7.6 years (dust flux-derived; Saito & Moffett, 2002). A recent global ocean model estimate of 7 years for Co τ_{Tot} in the upper 250 m matches well with our full transect τ_{Tot} average for the upper 200 m of 9 years (Tagliabue et al., 2018). Previous Mn estimates for the Pacific and Atlantic have ranged from a few years to 20 years (Landing & Bruland, 1987; Martin & Knauer, 1984; Martin et al., 1985, 1980; Shiller, 1997). A single trap study from the South China Sea reported τ_{Tot} on the order of 1 to 3 months for biogenic Cd and P (Ho et al., 2009), shorter than what was estimated on this transect. Considering the wide range in study locations and methods, the broad agreement in these numbers is promising.

The τ_{Tot} results show that P remains in the upper 100 m a bit longer (0.5–13 years) than Co and Cd (0.1 − years), but overall, these more nutrient-like components have zonal τ_{Tot} averages on the order of years (Table 1). Mn τ_{Tot}, despite being controlled by different processes, also falls in this range. The similarity in these τ_{Tot} values is unsurprising considering the partitioning of the total inventory of each component in the upper 100 m. The large particle pool composes, on average, 1–2% of the total pool for Mn, Co, and P and the percentage for Cd is slightly higher at 6%. Because the large particle pool is a greater contributor for Cd, sinking particle fluxes have a greater impact and τ_{Tot} values are shorter. Cd τ_{Tot} values are slightly shorter in the Offshore and Gyre than those for Co and Mn.

The total residence time with respect to export in the upper 200 m (Figure 3) reflects the balance of processes removing each component from the particulate pool, like remineralization, and the affinity of particles for a component. Longer τ_{Tot} estimates indicate that precipitation and scavenging rates are low with respect to remineralization rates. Although τ_{Tot} values are relatively similar in the Shelf and Offshore for Cd, Co, and Mn, the much shorter τ_{Tot} for Mn in the Gyre (1 year) shows the greater importance of scavenging and/or precipitation to Mn distributions and remineralization processes to Cd and Co distributions (τ_{Tot} = 8 and 4 years).

In determining τ_{Tot} with respect to export, we assume that the particulate export flux represents the net removal of TM from a depth horizon; however, the much longer 0- to 200-m τ_{Tot} estimates for Cd and Co in the Offshore suggest that physical transport processes, such as advection, could play a role in setting the absolute residence time of TM in this zone. In fact, high ^{228}Ra at station 9 (which is driving the high mean τ_{Tot}) suggests that this water had recent contact with the shelf and likely was transported by an eddy (Sanial et al., 2018). The 0- to 200-m Mn τ_{Tot} for this zone, however, does not include data from station 9 (flux = uncertainty), and the τ_{Tot} is still triple that of the Shelf and much larger than the τ_{Tot} for the Gyre. Therefore, the eddy station does not fully account for the longer τ_{Tot} in the 0–200 m Offshore. Without additional estimates of dissolved fluxes to and from each of the zones, especially in the N-S direction, we cannot determine the degree to which they may impact local additions or removals of the total TM inventory. However, if

the net TM removal via offshore transport does surpass the amount of TM removal via export in a given region, the τ_{Tot} determined with respect to particulate export would appear longer and, thus, can be considered upper limits of the absolute τ_{Tot}.

5. Conclusions

This study provides a comprehensive description of the comparative cycling of POC and particulate P, Cd, Co, and Mn in the eastern tropical South Pacific. Key patterns emerge within the three biogeochemical zones of the transect for the fluxes of each component. P and Cd behave the most "biologically," that is, similar to POC, with nutrient-like particulate and dissolved profiles and flux distributions that reflect production and remineralization of organic matter. Mn is characterized as the most authigenic-lithogenic TM of the group, with concentration and particulate flux profiles shaped by precipitation and/or scavenging in the subsurface waters of the Gyre and reduction in the sunlit upper ocean and the ODZ. Although the export of Co in the upper 200 m of this region mostly reflects nutrient-like properties, Co can be considered a hybrid element based on the scavenging-like export patterns observed in the Gyre (Saito et al., 2017).

Although it has been suggested that whole-ocean residence times could be "governed largely by processes occurring either in near-surface waters or at ocean margins" (Sherrell & Boyle, 1992), nonaerosol-based flux and residence time studies for TM in upper 400 m of the ocean are scarce. This study illustrates the benefit of cosampling for particulate TM and ^{234}Th and has produced some of the first large-scale ^{234}Th-derived flux and surface residence time estimates for TM in the global ocean. These estimates will help to close TM budgets for the Pacific Ocean, and we anticipate that these data will aid in the improvement of current OBGCMs used to model dissolved and particulate TM distributions, especially in the Pacific OMZ, where OBGCMs struggle to reproduce in situ distributions (van Hulten et al., 2017). The ^{234}Th method for determining the residence time of TM in the surface ocean provides a useful alternative to dust-based estimates, where observation-based fluxes have been shown to disagree by 2 orders of magnitude in some cases (Anderson et al., 2016).

There are many opportunities to carry this ^{234}Th-based technique forward. As of this publication, the GEOTRACES program has already provided a platform for paired ^{234}Th-TM sampling in the North Atlantic (GA03 and GA01), Southern Pacific (this transect GP-16), the western Arctic (GN01), the Mediterranean Sea (GA04), and the Kerguelen Plateau (Glpr01). In addition, many more TM than Cd, Co, and Mn have been measured during these cruises and the ^{234}Th method could provide the first estimates of surface export for some of the rarer TM. Recommendations for future campaigns include (1) sampling component:^{234}Th ratios at multiple depths in the upper 300 m, spaced to capture both relevant features (like an ODZ or deep chlorophyll maxima) and to maintain evenly spaced intervals; (2) utilizing multiple radiotracer systems to capture processes over varying time scales to integrate estimates for both dissolved and particulate pools; and (3) incorporating a paired trap and ^{234}Th flux process study to determine what types of particles contribute to the sinking flux of TM.

Acknowledgments
This work was supported by the National Science Foundation (OCE-1232669 and OCE-1518110), and Erin Black was also funded by a NASA Earth and Space Science Graduate Fellowship (NNX13AP31H). The authors would like to thank the captain, crew, and scientists aboard the R/V *Thomas G. Thompson*. A special thanks to two anonymous reviewers and Virginie Sanial for providing the additional ^{228}Ra-based estimates for Cd. All original data have been made available in either the supporting information or through BCO-DMO (see Website and Database References).

References

Albani, S., Mahowald, N. M., Perry, A. T., Scanza, R. A., Zender, C. S., Heavens, N. G., et al. (2014). Improved dust representation in the Community Atmosphere Model. *Journal of Advances in Modeling Earth Systems*, *6*, 541–570. https://doi.org/10.1002/2013MS000279

Anderson, R. F., Cheng, H., Edwards, R. L., Fleisher, M. Q., Hayes, C. T., Huang, K., et al. (2016). How well can we quantify dust deposition to the ocean? *Philosophical Transactions of the Royal Society A*, *374*(2081), 26. https://doi.org/10.1098/rsta.2015.0285

Benitez-Nelson, C., Buesseler, K. O., Karl, D. M., & Andrews, J. (2001). A time-series study of particulate matter export in the North Pacific Subtropical Gyre based on ^{234}Th:^{238}U disequilibrium. *Deep Sea Research, Part I*, *48*(12), 2595–2611. https://doi.org/10.1016/S0967-0637(01)00032-2

Benitez-Nelson, C. R., & Buesseler, K. O. (1999). Variability of inorganic and organic phosphorus turnover rates in the coastal ocean. *Nature*, *398*(6727), 502–505. https://doi.org/10.1038/19061

Benitez-Nelson, C. R., O'Neill Madden, L. P., Styles, R. M., Thunell, R. C., & Astor, Y. (2007). Inorganic and organic sinking particulate phosphorus fluxes across the oxic/anoxic water column of Cariaco Basin, Venezuela. *Marine Chemistry*, *105*(1–2), 90–100. https://doi.org/10.1016/j.marchem.2007.01.007

Bishop, J. K., Edmond, J. M., Ketten, D. R., Bacon, M. P., & Silker, W. B. (1977). The chemistry, biology, and vertical flux of particulate matter from the upper 400 m of the equatorial Atlantic Ocean. *Deep-Sea Research*, *24*(6), 511–548. https://doi.org/10.1016/0146-6291(77)90526-4

Bishop, J. K. B., & Fleisher, M. Q. (1987). Particulate manganese dynamics in Gulf Stream warm-core rings and surrounding waters of the N.W. Atlantic. *Geochimica et Cosmochimica Acta*, *51*(10), 2807–2825. https://doi.org/10.1016/0016-7037(87)90160-8

Bishop, J. K. B., Lam, P. J., & Wood, T. J. (2012). Getting good particles: Accurate sampling of particles by large volume in-situ filtration. *Limnology and Oceanography: Methods*, *10*(9), 681–710. https://doi.org/10.4319/lom.2012.10.681

Black, E. E., Buesseler, K. O., Pike, S. M., & Lam, P. J. (2018). ^{234}Th as a tracer of particulate export and remineralization in the southeastern tropical Pacific. *Marine Chemistry*, *201*, 35–50. https://doi.org/10.1016/j.marchem.2017.06.009

Bowie, A. R., Lannuzel, D., Remenyi, T. A., Wagener, T., Lam, P. J., Boyd, P. W., et al. (2009). Biogeochemical iron budgets of the Southern Ocean south of Australia: Decoupling of iron and nutrient cycles in the subantarctic zone by the summertime supply. *Global Biogeochemical Cycles*, *23*, GB4034. https://doi.org/10.1029/2009GB003500

Bown, J., Boye, M., Baker, A., Duvieilbourg, E., Lacan, F., Le Moigne, F., et al. (2011). The biogeochemical cycle of dissolved cobalt in the Atlantic and the Southern Ocean south off the coast of South Africa. *Marine Chemistry*, *126*(1–4), 193–206. https://doi.org/10.1016/j.marchem.2011.03.008

Boyle, E. A. (1988). Cadmium: Chemical tracer of deepwater paleoceanography. *Paleoceanography*, *3*(4), 471–489. https://doi.org/10.1029/PA003i004p00471

Bruland, K. W., & Lohan, M. C. (2003). Controls of trace metals in seawater. In H. D. Holland, & K. K. Turekian (Eds.), *The oceans and marine geochemistry* (chap. 6.02, Vol. 6, pp. 23–47) Oxford, UK: Elsevier Ltd.

Bruland, K. W., Orians, K. J., & Cowen, J. P. (1994). Reactive trace metals in the stratified central North Pacific. *Geochimica et Cosmochimica Acta*, *58*(15), 3171–3182. https://doi.org/10.1016/0016-7037(94)90044-2

Buesseler, K. O., Bacon, M. P., Cochrant, J. K., & Livingston, H. D. (1992). Carbon and nitrogen export during the JGOFS North Atlantic bloom experiment estimated from ^{234}Th:^{238}U disequilibria. *Deep-Sea Research*, *39*(7–8), 1115–1137. https://doi.org/10.1016/0198-0149(92)90060-7

Buesseler, K. O., Benitez-Nelson, C. R., Moran, S. B., Burd, A., Charette, M., Cochran, J. K., et al. (2006). An assessment of particulate organic carbon to thorium-234 ratios in the ocean and their impact on the application of ^{234}Th as a POC flux proxy. *Marine Chemistry*, *100*(3-4), 213–233. https://doi.org/10.1016/j.marchem.2005.10.013

Buesseler, K. O., & Boyd, P. W. (2009). Shedding light on processes that control particle export and flux attenuation in the twilight zone of the open ocean. *Limnology and Oceanography*, *54*(4), 1210–1232. https://doi.org/10.4319/lo.2009.54.4.1210

Buesseler, K. O., Jayne, S. R., Fisher, N. S., Rypina, I. I., Baumann, H., Baumann, Z., et al. (2012). Fukushima-derived radionuclides in the ocean and biota off Japan. *Proceedings of the National Academy of Sciences*, *109*(16), 5984–5988. https://doi.org/10.1073/pnas.1120794109

Buesseler, K. O., Pike, S., Maiti, K., Lamborg, C. H., Siegel, D. A., & Trull, T. W. (2009). Thorium-234 as a tracer of spatial, temporal and vertical variability in particle flux in the North Pacific. *Deep Sea Research, Part I*, *56*(7), 1143–1167. https://doi.org/10.1016/j.dsr.2009.04.001

Collier, R., Dymond, J., Honjo, S., Manganini, S., Francois, R., & Dunbar, R. (2000). The vertical flux of biogenic and lithogenic material in the Ross Sea: Moored sediment trap observations 1996–1998. *Deep Sea Research, Part II*, *47*(15–16), 3491–3520. https://doi.org/10.1016/S0967-0645(00)00076-X

Cowen, J. P., & Bruland, K. W. (1985). Metal deposits associated with bacteria: Implications for Fe and Mn marine biogeochemistry. *Deep Sea Research*, *32*(3), 253–272. https://doi.org/10.1016/0198-0149(85)90078-0

Cullen, J. T., & Sherrell, R. M. (1999). Techniques for determination of trace metals in small samples of size-fractionated particulate matter: Phytoplankton metals off central California. *Marine Chemistry*, *67*(3–4), 233–247. https://doi.org/10.1016/S0304-4203(99)00060-2

Cutter, G. A., Moffett, J. W., Nielsdottir, M., & Sanial, V. (2018). Multiple oxidation state trace elements in low oxygen waters of Peru: In situ redox processes and horizontal advective/diffusive transport. *Marine Chemistry*, *201*, 77–89. https://doi.org/10.1016/j.marchem.2018.01.003

de Baar, H. J. W., Saager, P. M., Nolting, R. F., & van der Meer, J. (1994). Cadmium versus phosphate in the world ocean. *Marine Chemistry*, *46*(3), 261–281. https://doi.org/10.1016/0304-4203(94)90082-5

Dehairs, F., Fagel, N., Antia, A. N., Peitner, R., Elskens, M., & Goeyens, L. (2000). Export production in the Bay ofd Biscay as estimated from barium-barite in settling material: a comparison with new production. *Deep-Sea Research*, *47*(4), 583–601. https://doi.org/10.1016/S0967-0637(99)00072-2

Dulaquais, G., Boye, M., Middag, R., Owens, S., Puigcorbé, V., Buesseler, K. O., et al. (2014). Contrasting biochemical cycles of cobalt in the surface western Atlantic Ocean. *Global Biogeochemical Cycles*, *28*, 1387–1412. https://doi.org/10.1002/2014GB004903.Received

Dunne, J. P., Murray, J. W., Young, J., Balistrieri, L. S., & Bishop, J. (1997). Th-234 and particle cycling in the central equatorial Pacific. *Deep - Sea Research Part II - Topical Studies in Oceanography*, *44*(9–10), 2049–2083. https://doi.org/10.1016/S0967-0645(97)00063-5

Durkin, C. A., Estapa, M. L., & Buesseler, K. O. (2015). Observations of carbon export by small sinking particles in the upper mesopelagic. *Marine Chemistry*, *175*, 72–81. https://doi.org/10.1016/j.marchem.2015.02.011

Dymond, J., & Collier, R. (1996). Particulate barium fluxes and their relationships to biological productivity. *Deep Sea Research, Part II*, *43*(4–6), 1283–1308. https://doi.org/10.1016/0967-0645(96)00011-2

Elderfield, H., & Rickaby, R. (2000). Oceanic Cd/P ratio and nutrient utilization in the glacial Southern Ocean. *Nature*, *405*(6784), 305–310. https://doi.org/10.1038/35012507

Ellwood, M. J., Nodder, S. D., King, A. L., Hutchins, D. A., Wilhelm, S. W., & Boyd, P. W. (2014). Pelagic iron cycling during the subtropical spring bloom, east of New Zealand. *Marine Chemistry*, *160*, 18–33. https://doi.org/10.1016/j.marchem.2014.01.004

Fiedler, P. C., & Talley, L. D. (2006). Hydrography of the eastern tropical Pacific: A review. *Progress in Oceanography*, *69*(2-4), 143–180. https://doi.org/10.1016/j.pocean.2006.03.008

Francis, C. A., Co, E. M., & Tebo, B. M. (2001). Enzymatic manganese (II) oxidation by a marine alpha-Proteobacterium. *Applied and Environmental Microbiology*, *67*(9), 4024–4029. https://doi.org/10.1128/AEM.67.9.4024

Frew, R. D., Hutchins, D. A., Nodder, S., Sanudo-Wilhelmy, S., Tovar-Sanchez, A., Leblanc, K., et al. (2006). Particulate iron dynamics during Fe cycle in subantarctic waters southeast of New Zealand. *Global Biogeochemical Cycles*, *20*, GB1S93. https://doi.org/10.1029/2005GB002558

Hatta, M., Measures, C. I., Wu, J., Roshan, S., Fitzsimmons, J. N., Sedwick, P., & Morton, P. (2015). An overview of dissolved Fe and Mn distributions during the 2010–2011 U.S. GEOTRACES North Atlantic cruises: GEOTRACES GA03. *Deep Sea Research, Part II*, *116*, 117–129. https://doi.org/10.1016/j.dsr2.2014.07.005

Hawco, N. J., Lam, P. J., Lee, J. M., Ohnemus, D. C., Noble, A. E., Wyatt, N. J., et al. (2018). Cobalt scavenging in the mesopelagic ocean and its influence on global mass balance: Synthesizing water column and sedimentary fluxes. *Marine Chemistry*, *201*, 151–166. https://doi.org/10.1016/j.marchem.2017.09.001

Hawco, N. J., Ohnemus, D. C., Resing, J. A., Twining, B. S., & Saito, M. A. (2016). A dissolved cobalt plume in the oxygen minimum zone of the eastern tropical South Pacific. *Biogeosciences*, *13*(20), 5697–5717. https://doi.org/10.5194/bg-13-5697-2016

Ho, T. Y., You, C. F., Chou, W. C., Pai, S. C., Wen, L. S., & Sheu, D. D. (2009). Cadmium and phosphorus cycling in the water column of the South China Sea: The roles of biotic and abiotic particles. *Marine Chemistry*, *115*(1–2), 125–133. https://doi.org/10.1016/j.marchem.2009.07.005

Horner, T. J., Lee, R. B. Y., Henderson, G. M., & Rickaby, R. E. M. (2013). Nonspecific uptake and homeostasis drive the oceanic cadmium cycle. *Proceedings of the National Academy of Sciences*, *110*(7), 2500–2505. https://doi.org/10.1073/pnas.1213857110

Hung, C. C., Gong, G. C., & Santschi, P. H. (2012). ^{234}Th in different size classes of sediment trap collected particles from the northwestern Pacific Ocean. *Geochimica et Cosmochimica Acta*, *91*, 60–74. https://doi.org/10.1016/j.gca.2012.05.017

Janssen, D. J., Conway, T. M., John, S. G., Christian, J. R., Kramer, D. I., Pedersen, T. F., & Cullen, J. T. (2014). Undocumented water column sink for cadmium in open ocean oxygen-deficient zones. *Proceedings of the National Academy of Sciences*, *111*(19), 6888–6893. https://doi.org/10.1073/pnas.1402388111

Jeandel, C., Tachikawa, K., Bory, A., & Dehairs, F. (2000). Biogenic barium in suspended and trapped material as a tracer of export production in the tropical NE Atlantic (EUMELI sites). *Marine Chemistry*, *71*(1–2), 125–142. https://doi.org/10.1016/S0304-4203(00)00045-1

Jickells, T. D., An, Z. S., Andersen, K. K., Baker, A. R., Bergametti, G., Brooks, N., et al. (2005). Global iron connections between desert dust, ocean biogeochemistry, and climate. *Science*, *308*, 67–72.

John, S. G., Helgoe, J., & Townsend, E. (2018). Biogeochemical cycling of Zn and Cd and their stable isotopes in the eastern tropical South Pacific. *Marine Chemistry*, *201*, 256–262. https://doi.org/10.1016/j.marchem.2017.06.001

Johnson, K. S., Berelson, W. M., Coale, K. H., Coley, T. L., Elrod, V. A., Fairey, W. R., et al. (1992). Manganese flux from continental margin sediments in a transect through the oxygen minimum. *Science*, *257*(5074), 1242–1245. https://doi.org/10.1126/science.257.5074.1242

Kadko, D. (2017). Upwelling and primary production during the U.S. GEOTRACES East Pacific zonal transect. *Global Biogeochemical Cycles*, *31*, 1–15. https://doi.org/10.1002/2016GB005554

Karstensen, J., Stramma, L., & Visbeck, M. (2008). Oxygen minimum zones in the eastern tropical Atlantic and Pacific Oceans. *Progress in Oceanography*, *77*(4), 331–350. https://doi.org/10.1016/j.pocean.2007.05.009

Lam, P. J., & Bishop, J. K. B. (2008). The continental margin is a key source of iron to the HNLC North Pacific Ocean. *Geophysical Research Letters*, *35*, L07608. https://doi.org/10.1029/2008GL033294

Lam, P. J., Bishop, J. K. B., Henning, C. C., Marcus, M. A., Waychunas, G. A., & Fung, I. Y. (2006). Wintertime phytoplankton bloom in the subarctic Pacific supported by continental margin iron. *Global Biogeochemical Cycles*, *20*, GB1006. https://doi.org/10.1029/2005GB002557

Lam, P. J., Lee, J. M., Heller, M. I., Mehic, S., Xiang, Y., & Bates, N. R. (2018). Size-fractionated distributions of suspended particle concentration and major phase composition from the U.S. GEOTRACES eastern Pacific zonal transect (GP16). *Marine Chemistry*, *201*, 90–107. https://doi.org/10.1016/j.marchem.2017.08.013

Lam, P. J., Ohnemus, D. C., & Auro, M. E. (2015). Size-fractionated major particle composition and concentrations from the US GEOTRACES North Atlantic zonal transect. *Deep Sea Research, Part II*, *116*, 303–320. https://doi.org/10.1016/j.dsr2.2014.11.020

Lamborg, C. H., Buesseler, K. O., & Lam, P. J. (2008). Sinking fluxes of minor and trace elements in the North Pacific Ocean measured during the VERTIGO program. *Deep-Sea Research Part II: Topical Studies in Oceanography*, *55*(14–15), 1564–1577. https://doi.org/10.1016/j.dsr2.2008.04.012

Lamborg, C. H., Hammerschmidt, C. R., Bowman, K. L., Swarr, G. J., Munson, K. M., Ohnemus, D. C., et al. (2014). A global ocean inventory of anthropogenic mercury based on water column measurements. *Nature*, *512*(7512), 65–68. https://doi.org/10.1038/nature13563

Landing, W. M., & Bruland, K. W. (1987). The contrasting biogeochemistry of manganese and iron in the Pacific Ocean. *Geochimica et Cosmochimica Acta*, *51*(1), 29–43. https://doi.org/10.1016/0016-7037(87)90004-4

Law, G. T. W., Shimmield, T. M., Shimmield, G. B., Cowie, G. L., Breuer, E. R., & Martyn Harvey, S. (2009). Manganese, iron, and sulphur cycling on the Pakistan margin. *Deep-Sea Research Part II: Topical Studies in Oceanography*, *56*(6–7), 305–323. https://doi.org/10.1016/j.dsr2.2008.06.011

Lee, J. M., Heller, M. I., & Lam, P. J. (2018). Size distribution of particulate trace elements in the U.S. GEOTRACES eastern Pacific zonal transect (GP16). *Marine Chemistry*, *201*, 108–123. https://doi.org/10.1016/j.marchem.2017.09.006

Lemaitre, N., Planquette, H., Dehairs, F., van der Merwe, P., Bowie, A. R., Trull, T. W., et al. (2016). Impact of the natural Fe-fertilization on the magnitude, stoichiometry and efficiency of particulate biogenic silica, nitrogen and iron export fluxes. *Deep Sea Research, Part I*, *117*, 11–27. https://doi.org/10.1016/j.dsr.2016.09.002

Martin, J. H., & Knauer, G. A. (1983). VERTEX: Manganese transport with $CaCO_3$. *Deep-Sea Research*, *30*(4), 411–425. https://doi.org/10.1016/0198-0149(83)90075-4

Martin, J. H., & Knauer, G. A. (1984). VERTEX: Manganese transport through oxygen minima. *Earth and Planetary Science Letters*, *67*(1), 35–47. https://doi.org/10.1016/0012-821X(84)90036-0

Martin, J. H., Knauer, G. A., & Broenkow, W. W. (1985). VERTEX: The lateral transport of manganese in the northeast Pacific. *Deep Sea Research Part A, Oceanographic Research Papers*, *32*(11), 1405–1427. https://doi.org/10.1016/0198-0149(85)90056-1

Martin, J. H., Knauer, G. A., Landing, M., Laboratories, M., Landing, M., & Ca, U. S. A. (1980). Manganese cycling in Northeast Pacific waters. *Earth and Planetary Science Letters*, *51*(2), 266–274. https://doi.org/10.1016/0012-821X(80)90209-5

Martínez-García, A., Sigman, D. M., Ren, H., Anderson, R. F., Straub, M., Hodell, D. A., et al. (2014). Iron fertilization of the Subantarctic Ocean during the last ice age. *Science*, *343*(6177), 1347–1350. https://doi.org/10.1126/science.1246848

Martiny, A. C., Pham, C. T. A., Primeau, F. W., Vrugt, J. A., Moore, J. K., Levin, S. A., & Lomas, M. W. (2013). Strong latitudinal patterns in the elemental ratios of marine plankton and organic matter. *Nature Geoscience*, *6*(4), 279–283. https://doi.org/10.1038/ngeo1757

McManus, J., Berelson, W. M., Severmann, S., Johnson, K. S., Hammond, D. E., Moutusi, R., & Coale, K. H. (2012). Benthic manganese fluxes along the Oregon and California continental shelf and slope. *Continental Shelf Research*, *43*, 71–85. https://doi.org/10.1016/j.csr.2012.04.016

McManus, J., Dymond, J., Dunbar, R. B., & Collier, R. W. (2002). Particulate barium fluxes in the Ross Sea. *Marine Geology*, *184*(1–2), 1–15. https://doi.org/10.1016/S0025-3227(01)00300-0

Migon, C., Sandroni, V., Marty, J. C., Gasser, B., & Miquel, J. C. (2002). Transfer of atmospheric matter through the euphotic layer in the northwestern Mediterranean: Seasonal pattern and driving forces. *Deep Sea Research, Part II*, *49*(11), 2125–2141. https://doi.org/10.1016/S0967-0645(02)00031-0

Moffett, J. W. (1990). Microbially mediated cerium oxidation in sea water. *Nature*, *345*(6274), 421–423. https://doi.org/10.1038/345421a0

Moffett, J. W., & Ho, J. (1996). Oxidation of cobalt and manganese in seawater via a common microbially catalyzed pathway. *Geochimica et Cosmochimica Acta*, *60*(18), 3415–3424. https://doi.org/10.1016/0016-7037(96)00176-7

Moore, C. M., Mills, M. M., Arrigo, K. R., Berman-Frank, I., Bopp, L., Boyd, P. W., et al. (2013). Processes and patterns of oceanic nutrient limitation. *Nature Geoscience*, *6*(9), 701–710. https://doi.org/10.1038/ngeo1765

Morel, F. M. M., Milligan, A. J., & Saito, M. A. (2004). Marine bioinorganic chemistry: The role of trace metals in the oceanic cycles of major nutrients. In H. Elderfield (Ed.), *Treatise on geochemistry*, (Vol. 6, pp. 113–143). Oxford, UK: Elsevier Ltd.

Morel, F. M. M., & Price, N. M. (2003). The biogeochemical cycles of trace metals in the oceans. *Science*, *300*(5621), 944–947. https://doi.org/10.1126/science.1083545

Noble, A. E., Lamborg, C. H., Ohnemus, D. C., Lam, P. J., Goepfert, T. J., Measures, C. I., et al. (2012). Basin-scale inputs of cobalt, iron, and manganese from the Benguela-Angola front to the South Atlantic Ocean. *Limnology and Oceanography*, *57*(4), 989–1010. https://doi.org/10.4319/lo.2012.57.4.0989

Not, C., Brown, K. A., Ghaleb, B., & Hillaire-Marcel, C. (2012). Conservative behavior of uranium vs. salinity in Arctic Sea ice and brine. *Marine Chemistry*, *130-131*, 33–39. https://doi.org/10.1016/j.marchem.2011.12.005

Ohnemus, D. C., Rauschenberg, S., Cutter, G. A., Fitzsimmons, J. N., Sherrell, R. M., & Twining, B. S. (2016). Elevated trace metal content of prokaryotic plankton communities associated with marine oxygen deficient zones. *Limnology and Oceanography*, *62*(1), 3–25. https://doi.org/10.1002/lno.10363

Owens, S. A., Buesseler, K. O., & Sims, K. W. W. (2011). Re-evaluating the ^{238}U-salinity relationship in seawater: Implications for the ^{238}U–^{234}Th disequilibrium method. *Marine Chemistry*, *127*(1-4), 31–39. https://doi.org/10.1016/j.marchem.2011.07.005

Owens, S. A., Pike, S., & Buesseler, K. O. (2015). Thorium-234 as a tracer of particle dynamics and upper ocean export in the Atlantic Ocean. *Deep Sea Research, Part II*, *116*, 42–59. https://doi.org/10.1016/j.dsr2.2014.11.010

Passow, U., Dunne, J., Murray, J. W., Balistrieri, L., & Alldredge, A. L. (2006). Organic carbon to ^{234}Th ratios of marine organic matter. *Marine Chemistry*, *100*(3-4), 323–336. https://doi.org/10.1016/j.marchem.2005.10.020

Planquette, H., Sanders, R. R., Statham, P. J., Morris, P. J., & Fones, G. R. (2011). Fluxes of particulate iron from the upper ocean around the Crozet Islands: A naturally iron-fertilized environment in the Southern Ocean. *Global Biogeochemical Cycles*, *25*, GB2011. https://doi.org/10.1029/2010GB003789

Pohl, C., Löffler, A., & Hennings, U. (2004). A sediment trap flux study for trace metals under seasonal aspects in the stratified Baltic Sea (Gotland Basin; 57°19.20′N; 20°03.00′E). *Marine Chemistry*, *84*(3–4), 143–160. https://doi.org/10.1016/j.marchem.2003.07.002

Puigcorbé, V., Benitez-nelson, C. R., Masqué, P., Verdeny, E., White, A. E., Popp, B. N., et al. (2015). Small phytoplankton drive high summertime carbon and nutrient export in the Gulf of California and eastern tropical North Pacific. *Global Biogeochemical Cycles*, *29*, 1309–1332. https://doi.org/10.1002/2015GB005134

Quetel, C. R., Remoudaki, E., Davies, J. E., Miquel, J. C., Fowler, S. W., Lambert, C. E., et al. (1993). Impact of atmospheric deposition on particulate iron flux and distribution in northwestern Mediterranean waters. *Deep Sea Research, Part I*, *40*(5), 989–1002. https://doi.org/10.1016/0967-0637(93)90085-H

Resing, J. A., Sedwick, P. N., German, C. R., Jenkins, W. J., Moffett, J. W., Sohst, B. M., & Tagliabue, A. (2015). Basin-scale transport of hydrothermal dissolved metals across the South Pacific Ocean. *Nature*, *523*(7559), 200–203. https://doi.org/10.1038/nature14577

Rosenthal, Y., Lam, P. J., Boyle, E. A., & Thompson, J. (1995). Authigenic cadmium enrichments in suboxic sediments: Precipitation and postdepositional mobility. *Earth and Planetary Science Letters*, *132*(1–4), 99–111. https://doi.org/10.1016/0012-821X(95)00056-I

Saito, M. A., & Goepfert, T. J. (2008). Zinc-cobalt colimitation of *Phaeocystis antarctica*. *Limnology and Oceanography*, *53*(1), 266–275. https://doi.org/10.4319/lo.2008.53.1.0266

Saito, M. A., & Moffett, J. W. (2002). Temporal and spatial variability of cobalt in the Atlantic Ocean. *Geochimica et Cosmochimica Acta*, *66*(11), 1943–1953. https://doi.org/10.1016/s0016-7037(02)00829-3

Saito, M. A., Moffett, J. W., & Ditullio, G. R. (2004). Cobalt and nickel in the Peru upwelling region: A major flux of labile cobalt utilized as a micronutrient. *Global Biogeochemical Cycles*, *18*, GB4030. https://doi.org/10.1029/2003GB002216

Saito, M. A., Noble, A. E., Hawco, N., Twining, B. S., Ohnemus, D. C., John, S. G., et al. (2017). The acceleration of dissolved cobalt's ecological stoichiometry due to biological uptake, remineralization, and scavenging in the Atlantic Ocean. *Biogeosciences*, *14*(20), 4637–4662. https://doi.org/10.5194/bg-14-4637-2017

Sanial, V., Kipp, L. E., Henderson, P. B., Van Beek, P., Reyss, J., Hammond, D. E., et al. (2018). Radium-228 as a tracer of dissolved trace element inputs from the Peruvian continental margin. *Marine Chemistry*, *201*, 20–34. https://doi.org/10.1016/j.marchem.2017.05.008

Scholz, F., Hensen, C., Noffke, A., Rohde, A., Liebetrau, V., & Wallmann, K. (2011). Early diagenesis of redox-sensitive trace metals in the Peru upwelling area—Response to ENSO-related oxygen fluctuations in the water column. *Geochimica et Cosmochimica Acta*, *75*(22), 7257–7276. https://doi.org/10.1016/j.gca.2011.08.007

Schüßler, U., Schulz-Bull, D. E., & Bauerfeind, E. (1997). Annual fluxes of particulate chemical trace compounds during the north-east water polynya experiment. *Journal of Marine Systems*, *10*(1–4), 391–400. https://doi.org/10.1016/S0924-7963(96)00077-2

Sherrell, R. M., & Boyle, A. (1992). The trace metal composition of suspended particles in the oceanic water column near Bermuda. *Earth and Planetary Science Letters*, *111*, 155–174.

Shiller, A. M. (1997). Manganese in surface waters of the Atlantic Ocean. *Geophysical Research Letters*, *24*(12), 1495–1498. https://doi.org/10.1029/97GL01456

Smith, J. N., Yeats, P. A., Knowlton, S. E., & Moran, S. B. (2014). Comparison of ^{234}Th/^{238}U and mass balance models for estimating metal removal fluxes in the Gulf of Maine and Scotian Shelf. *Continental Shelf Research*, *77*, 107–117. https://doi.org/10.1016/j.csr.2014.01.008

Stanley, R. H. R., Buesseler, K. O., Manganini, S. J., Steinberg, D. K., & Valdes, J. R. (2004). A comparison of major and minor elemental fluxes collected in neutrally buoyant and surface-tethered sediment traps. *Deep Sea Research, Part I*, *51*(10), 1387–1395. https://doi.org/10.1016/j.dsr.2004.05.010

Sunda, W. G., & Huntsman, S. A. (1987). Microbial oxidation of manganese in a North Carolina estuary. *Limnology and Oceanography*, *32*(3), 552–564. https://doi.org/10.4319/lo.1987.32.3.0552

Sunda, W. G., & Huntsman, S. A. (1994). Photoreduction of manganese oxides in seawater. *Marine Chemistry*, *46*(1–2), 133–152. https://doi.org/10.1016/0304-4203(94)90051-5

Sunda, W. G., & Huntsman, S. A. (1997). Interrelated influence of iron, light and cell size on marine phytoplankton growth. *Nature*, *2051*(1977), 389–392.

Tagliabue, A., Aumont, O., Death, R., Dunne, J. P., Dutkiewicz, S., Galbraith, E., et al. (2016). How well do global ocean biogeochemistry models simulate dissolved iron distributions? *Global Biogeochemical Cycles*, *30*, 149–174. https://doi.org/10.1002/2015GB005289

Tagliabue, A., Hawco, N. J., Bundy, R. M., Landing, W. M., Milne, A., Morton, P. L., & Saito, M. A. (2018). The role of external inputs and internal cycling in shaping the global ocean cobalt distribution: Insights from the first cobalt biogeochemical model. *Global Biogeochemical Cycles*, *32*, 594–616. https://doi.org/10.1002/2017GB005830

Taylor, S. ., & McLennan, S. (1995). The geochemical evolution of the continental crust. *Reviews of Geophysics*, *33*(2), 241–265. https://doi.org/10.1029/95RG00262

Tebo, B. M., Nealson, K. H., Emerson, S., & Jacobs, L. (1984). Microbial mediation of Mn (II) and Co (II) precipitation at the O_2/H_2S interfaces in two anoxic fjords. *Limnology and Oceanography*, *29*(6), 1247–1258. https://doi.org/10.4319/lo.1984.29.6.1247

Twining, B. S., & Baines, S. B. (2013). The trace metal composition of marine phytoplankton. *Annual Review of Marine Science*, *5*(1), 191–215. https://doi.org/10.1146/annurev-marine-121211-172322

Twining, B. S., Baines, S. B., Bozard, J. B., Vogt, S., Walker, E. A., & Nelson, D. M. (2011). Metal quotas of plankton in the equatorial Pacific Ocean. *Deep-Sea Research Part II: Topical Studies in Oceanography*, *58*(3–4), 325–341. http://doi.org/10.1016/j.dsr2.2010.08.018

Twining, B. S., Rauschenberg, S., Morton, P. L., Ohnemus, D. C., & Lam, P. J. (2015). Comparison of particulate trace element concentrations in the North Atlantic Ocean as determined with discrete bottle sampling and in situ pumping. *Deep Sea Research, Part II*, *116*, 273–282. https://doi.org/10.1016/j.dsr2.2014.11.005

van Hulten, M. M. P., Middag, R., Dutay, J.-C., de Baar, H. J. W., Roy-Barman, M., Gehlen, M., et al. (2017). Manganese in the West Atlantic Ocean in context of the first global ocean circulation model of manganese. *Biogeosciences*, *14*(5), 1123–1152. https://doi.org/10.5194/bg-14-1123-2017

Watson, A. J., Bakker, D. C. E., Ridgewell, A. J., Boyd, P. W., & Law, C. S. (2000). Effect of iron supply on Southern Ocean CO_2 uptake and implications for glacial atmospheric CO_2. *Nature*, *407*(6805), 730–733. https://doi.org/10.1038/35037561

Weinstein, S. E., & Moran, S. B. (2004). Distribution of size-fractionated particulate trace metals collected by bottles and in-situ pumps in the Gulf of Maine-Scotian Shelf and Labrador Sea. *Marine Chemistry*, *87*(3–4), 121–135. https://doi.org/10.1016/j.marchem.2004.02.004

Weinstein, S. E., & Moran, S. B. (2005). Vertical flux of particulate Al, Fe, Pb, and Ba from the upper ocean estimated from $^{234}Th/^{238}U$ disequilibria. *Deep Sea Research, Part I*, *52*(8), 1477–1488. https://doi.org/10.1016/j.dsr.2005.03.008

Website and Database References

Buesseler, K., Charette, M., & Moore, W. (2016). Th-234 from in-situ pumps, including large size fraction (>51 μm) and small size fraction (1–51 μm), from R/V *Thomas G. Thompson* cruise TN303 in the eastern tropical Pacific in 2013 (U.S. GEOTRACES EPZT project). Biological and chemical oceanography data management office (BCO-DMO). Dataset version: 2016-06-03. http://www.bco-dmo.org/dataset/643316

Buesseler, K., Charette, M., & Moore, W. (2017). Water-column total Th-234 and U-238 from R/V *Thomas G. Thompson* cruise TN303 in the eastern tropical Pacific in 2013 (U.S. GEOTRACES EPZT project). Biological and chemical oceanography data management office (BCO-DMO). Dataset version: 2017-01-27. http://www.bco-dmo.org/dataset/643213

John, S. (2015). Dissolved (0.4 micron filtered) Fe, Zn and Cd isotope ratios and concentrations across GEOTRACES-EPZT, from cruise TN303, 2013. Biological and chemical oceanography data management office (BCO-DMO). Dataset version 2016-06-21. http://lod.bco-dmo.org/id/dataset/643809

Lam, P. (2017). Size-fractionated major and minor particle composition and concentration collected from RV Thompson (TN303) along the US GEOTRACES EPZT transect in the eastern tropical Pacific during 2013 (US GEOTRACES EPZT project). Biological and chemical oceanography data management office (BCO-DMO). Dataset version 2017-01-03. http://lod.bco-dmo.org/id/dataset/668083

Moffett, J., German, C., and Cutter, G. (2014). ODF bottle data along the US GEOTRACES East Pacific zonal transect from the R/V *Thomas G. Thompson* TN303 cruise in the tropical Pacific from Peru to Tahiti during 2013 (U.S. GEOTRACES EPZT project). Biological and chemical oceanography data management office (BCO-DMO). Dataset version 2014-10-30. http://lod.bco-dmo.org/id/dataset/503145

NASA Goddard Space Flight Center, & Ocean Biology Processing Group (2018). *Moderate-Resolution Imaging Spectroradiometer (MODIS) Ocean Color Data*. Greenbelt, MD, USA: NASA OB.DAAC. https://oceandata.sci.gsfc.nasa.gov/MODIS-Aqua/Mapped/Annual/ [access date: 13 Apr 2018].

NOAA. (2009). World ocean atlas. https://www.nodc.noaa.gov/OC5/WOA09/pr_woa09.html [access date: 13 Apr 2018].

Resing, J. & Sedwick, P. (2016). Concentrations of dissolved manganese (Mn) in water-column samples from major stations that were occupied during the U.S. GEOTRACES EPZT cruise (R/V Thomas G. Thompson TN303) from October to December 2013. Biological and chemical oceanography data management office (BCO-DMO). Dataset version 2016-12-20. http://lod.bco-dmo.org/id/dataset/670692.

Saito, M. (2016). Total and labile dissolved cobalt from the GEOTRACES EPZT cruise. Biological and chemical oceanography data management office (BCO-DMO). Dataset version 2016-07-01. http://lod.bco-dmo.org/id/dataset/642974